RNA-binding protein Elavl1/HuR is required for maintenance of cranial neural crest specification

Erica J. Hutchins[1,4*], Shashank Gandhi[2], Jose Chacon[3], Michael L. Piacentino[1], and Marianne E. Bronner[1]

[1] Division of Biology & Biological Engineering, California Institute of Technology, Pasadena, CA 91125, USA.
[2] The Miller Institute for Basic Research in Science, University of California, Berkeley, Berkeley, CA , USA.
[3] Department of Biology, School of Math and Science, California State University Northridge, Northridge, CA 91330, USA.
[4] Present address: Department of Cell and Tissue Biology, University of California, San Francisco, San Francisco, CA 94143, USA.
*Correspondence: erica.hutchins@ucsf.edu

While neural crest development is known to be transcriptionally controlled via sequential activation of gene regulatory networks (GRNs), recent evidence increasingly implicates a role for post-transcriptional regulation in modulating the output of these regulatory circuits. Using available single cell RNA-sequencing datasets from avian embryos to identify potential post-transcriptional regulators, we found that *Elavl1*, which encodes for an RNA-binding protein with roles in transcript stability, was enriched in the premigratory cranial neural crest. Perturbation of Elavl1 resulted in premature neural crest delamination from the neural tube as well as significant reduction in transcripts associated with the neural crest specification GRN, phenotypes that are also observed with downregulation of the canonical Wnt inhibitor *Draxin*. That *Draxin* is the primary target for stabilization by Elavl1 during cranial neural crest specification was shown by RNA-sequencing, RNA-immunoprecipitation, RNA decay measurement and proximity ligation assays, further supporting the idea that the downregulation of neural crest specifier expression upon Elavl1 knockdown was largely due to loss of *Draxin*. Importantly, exogenous Draxin rescued cranial neural crest specification defects observed with Elavl1 knockdown. Thus, Elavl1 plays a critical a role in the maintenance of cranial neural crest specification via *Draxin* mRNA stabilization. Together, these data highlight an important intersection of post-transcriptional regulation with modulation of the neural crest specification GRN.

INTRODUCTION

Neural crest cells are an essential, multipotent cell population in the vertebrate embryo. During development, these cells undergo coordinated induction, specification, and epithelial—mesenchymal transition (EMT) events to migrate and ultimately form a myriad of tissues, including craniofacial structures, components of the peripheral nervous system, as well as many other derivatives (Gandhi and Bronner, 2018). The transcriptional control of these events has been dissected and mapped into modules of a feed-forward gene regulatory network (GRN), which helps explain the detailed sequence of events involved in neural crest development (Martik and Bronner, 2017; Simoes-Costa and Bronner, 2015; Williams et al., 2019). Recently, in addition to transcriptional events, there has been growing appreciation for the role that post-transcriptional regulation plays in the establishment, maintenance, and regulation of neural crest formation (Bhattacharya et al., 2018; Cibi et al., 2019; Copeland and Simoes-Costa, 2020; Forman et al., 2021; Sanchez-Vasquez et al., 2019; Ward et al., 2018; Weiner, 2018).

Given that RNA-binding proteins play an essential role in post-transcriptional regulatory processes (Dassi, 2017), we sought to broadly identify those with early roles in neural crest development. To this end, we analyzed existing single-cell RNA-sequencing data (Williams et al., 2019) from specification-stage avian embryos to identify enriched RNA-binding protein candidates. Using this approach, we identified *Elavl1* as an enriched transcript in newly formed neural crest cells. Elavl1 is a nucleocytoplasmic shuttling protein from the ELAV (embryonic lethal abnormal vision) family of RNA-binding proteins, which have conserved roles in neural development (Ma et al., 1996; Yao et al., 1993). It is a well-established stabilizer of mRNA, a function often mediated via association with the 3'-untranslated region (3'-UTR) of its mRNA targets (Abdelmohsen and Gorospe, 2010; Rothamel et al., 2021).

Elavl1 is essential for mammalian development and embryonic survival; Elavl1 null mouse embryos exhibit lethality due to abnormal placental morphogenesis, and conditional epiblast-null embryos display a broad array of phenotypes, ranging from defects in ossification and craniofacial development to asplenia. Interestingly, despite the myriad of tissue systems affected by Elavl1 knockout and relatively

broad expression in wild type embryos, mechanistic insights suggest Elavl1 acts on specific gene networks in a spatiotemporally controlled manner (Katsanou et al., 2009). Thus, due to its complexity and specificity of function, much remains to be discovered with respect to Elavl1's essential roles and targets during embryonic development across tissue-specific contexts.

Here, we sought to determine the role of Elavl1 during cranial neural crest specification by taking advantage of the chick embryo model, an amniote system in which it is possible to perturb Elavl1 function with precise spatiotemporal control via unilateral knock-down. The results show that perturbation of Elavl1 led to premature neural crest delamination, as well as significant reduction in the expression of genes within the neural crest specification GRN. We find that these effects were mediated by loss of *Draxin*, a direct mRNA target for stabilization by Elavl1. Our data demonstrate a critical role for Elavl1, and RNA-binding protein-mediated post-transcriptional control, in the regulation of a critical neural crest specification module.

RESULTS

The RNA-binding protein Elavl1 is expressed in cranial neural crest

Cranial neural crest cells are indispensable for proper craniofacial development (van Limborgh et al., 1983; Vega-Lopez et al., 2018). Whereas transcription factors have been well established critical regulators of neural crest development and craniofacial morphogenesis [reviewed in (Gou et al., 2015)], growing evidence indicates an essential role for post-transcriptional regulation in these processes (Cibi et al., 2019; Copeland and Simoes-Costa, 2020; Dennison et al., 2021; Forman et al., 2021). To identify RNA-binding proteins with potential roles in cranial neural crest specification, we analyzed single cell RNA-sequencing (scRNA-seq) data for cranial neural crest isolated from avian embryos at the 5-6 somite stage (Williams et al., 2019); we identified three distinct clusters (neural, premigratory (pNC), and delaminating/migratory (mNC)) among which genes associated with the gene ontology (GO) term "binds to 3' UTR" were differentially expressed (**Figure 1A-E**). To isolate potential positive regulators of neural crest specification, we then performed GO term analysis for "stabilizes RNA" and "regulates translation" among the identified RNA-binding proteins; only the *Elavl1* gene was associated with all three GO terms and abundantly expressed in the isolated cranial neural crest cells (**Figure 1F-G**).

Given that Elavl1 knockout mice often display defects in craniofacial structures (Katsanou et al., 2009), and the transcript appeared enriched in premigratory cranial neural crest cells (**Figure 1E**), we hypothesized a potential role for Elavl1 during cranial neural crest specification. To test this possibility, we first examined the expression pattern of Elavl1 in the developing chick embryo. Early in neurulation, when the neural plate border (NPB) is established within the rising neural folds, Elavl1 expression was detected in the anterior open neural tube and closing neural folds surrounding the anterior neuropore but absent from Pax7-expressing NPB cells (**Figure 2A**). As the neural tube closed, when neural crest specification is complete, Elavl1 expression became enriched throughout the neural tube and overlapped with Pax7 expression in premigratory cranial neural crest cells (**Figure 2B-D**). Following cranial neural crest epithelial—mesenchymal transition (EMT), Elavl1 remained expressed in the migratory neural crest cells, as well as throughout the brain and neural tube (**Figure 2E-G**). Thus, Elavl1 is expressed in specified, premigratory cranial neural crest cells following establishment of the NPB and is retained during the onset of EMT and in early migrating cranial neural crest cells.

Elavl1 downregulation alters cranial neural crest specification and delamination

To determine what, if any, role Elavl1 has in cranial neural crest specification, we perturbed Elavl1 function in the early embryo using a translation-blocking antisense morpholino oligo (MO). We electroporated control or Elavl1 MOs bilaterally into gastrula stage chick embryos and analyzed neural crest specification using quantitative fluorescent hybridization chain reaction (HCR) to measure expression of markers of specified neural crest at HH9 (**Figure 3A-B**). Given Elavl1's association with Wnt signaling (Kim et al., 2015) and the essential roles Wnt signaling plays during early neural crest development (Milet and Monsoro-Burq, 2012; Rabadán et al., 2016; Simoes-Costa and Bronner, 2015; Steventon and Mayor, 2012; Wu et al., 2003; Yanfeng et al., 2003), we focused on the Wnt effector *Axud1*, its target and neural crest specifier *FoxD3*, and the Wnt antagonist *Draxin* (Hutchins and Bronner, 2018, 2019; Simoes-Costa et al., 2015). Following Elavl1 knockdown (**Figure 3—Figure Supplement 1**; 61.4 ± 0.9% of the control side, $P < 0.001$, paired *t*-test, $n = 5$ embryos, 15 sections), we observed significant reduction in the levels of *Axud1* (**Figure 3C**; 73.7 ± 3.1% of the control side, $P = 0.03$, Wilcoxon signed-rank test, $n = 6$ embryos),

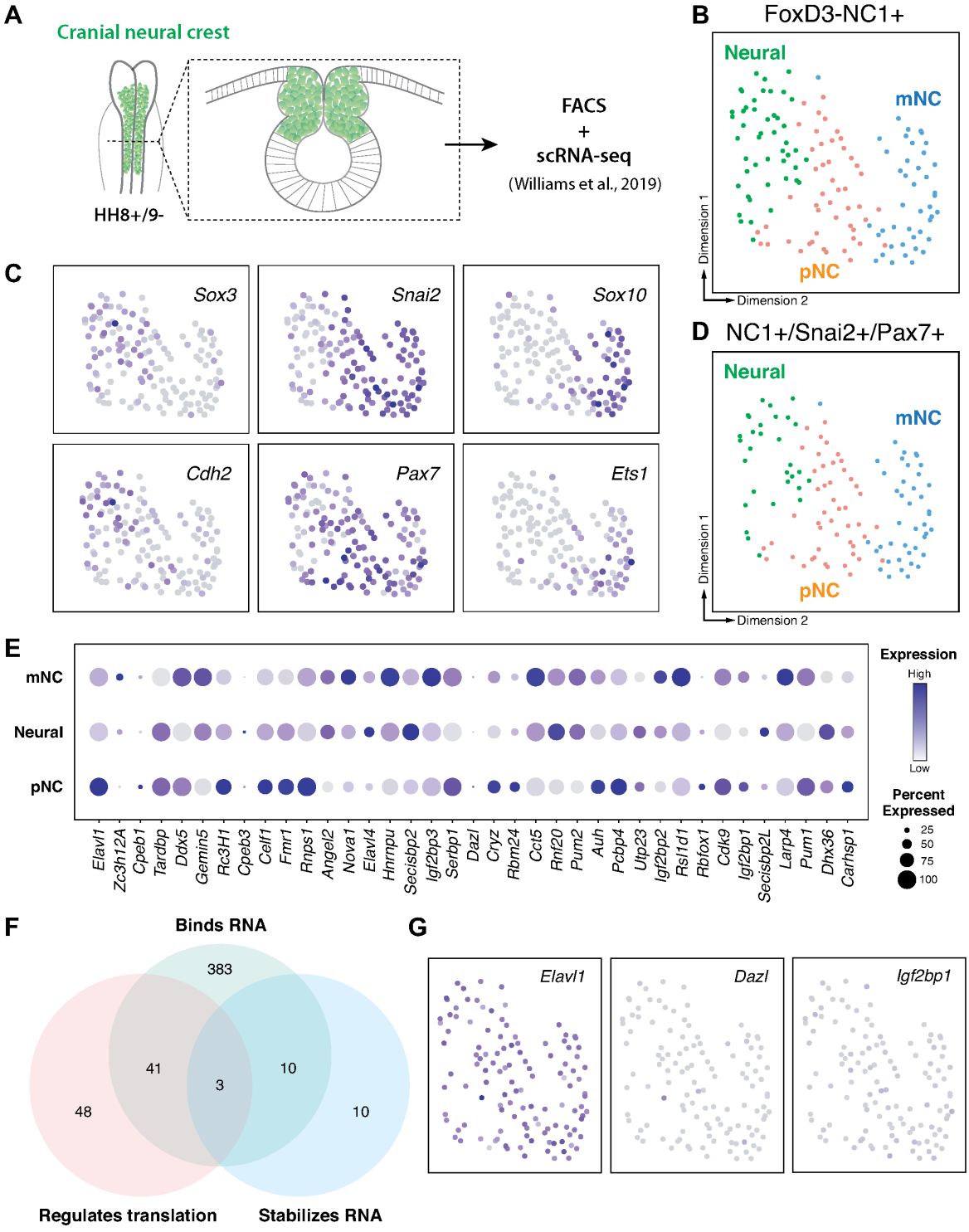

Figure 1. RNA-binding proteins are differentially expressed in premigratory and migratory cranial neural crest.
(**A**) Schematic of early chick cranial neural crest cells at premigratory stages (HH8+/9-) in intact heads and cross-section expressing Citrine fluorescent protein under control of the FoxD3 NC1 enhancer used by Williams and colleagues to sort cranial neural crest cells for single cell RNA-sequencing (scRNA-seq) (Williams et al., 2019). (**B-C**) Dimensionality reduction using Uniform Manifold Approximation and Projection (UMAP) on published scRNA-seq data from (Williams et al., 2019) identified three distinct clusters (neural, premigratory (pNC), and delaminating/migratory (mNC). Expression of marker genes (*Sox3* and *Cdh2* for neural, *Pax7* and *Snai2* for premigratory cranial neural crest, and *Sox10* and *Ets1* for early migratory cranial neural crest) was used to label the three sub-clusters. (**D**) The majority of the FoxD3-NC1+ cells were also positive for the expression of transcription factors *Pax7* and *Snai2*, which label the dorsal neural tube and premigratory/delaminating neural crest cells. These triple positive NC1+/Snai2+/Pax7+ were further processed for gene ontology analysis to identify post-transcriptional regulators. (**E**) A strip-plot showing expression and abundance of a subset of genes that are associated with the gene ontology term “binds to 3’ UTR.” (**F**) A three-way Venn diagram shows overlap between genes associated with the gene ontology terms “binds RNA,” “regulates translation,” and “stabilizes RNA.” Only three genes, *Elavl1*, *Dazl*, and *Igf2bp1*, were associated with all three. (**G**) Feature plots showing the expression distribution of the three genes identified in (**F**). Only *Elavl1* is abundant amongst all NC1+/Pax7+/Snai2+ cells.

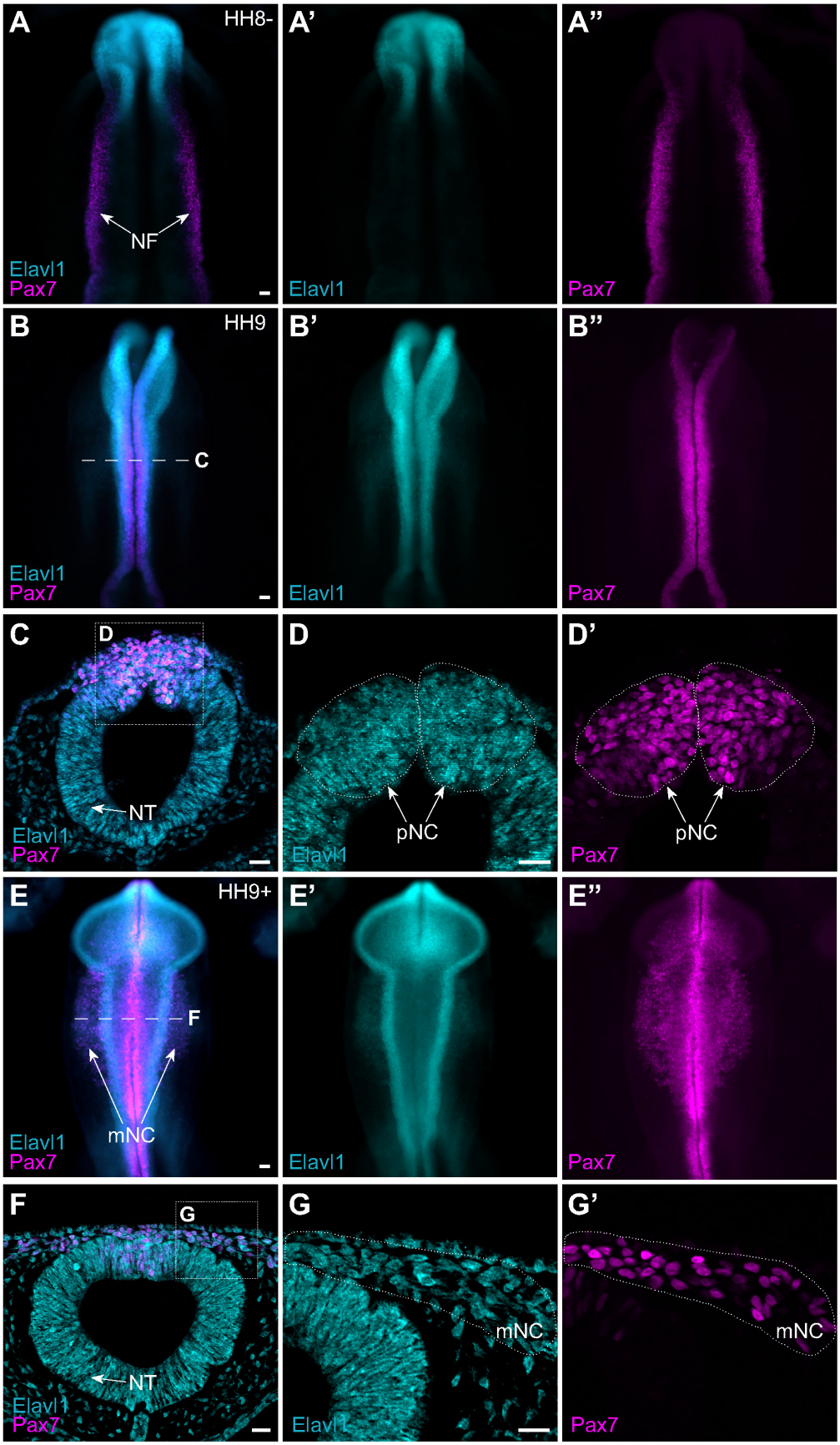

Figure 2. The RNA-binding protein Elavl1 is expressed in premigratory and migratory cranial neural crest.
(**A-G**) Representative epifluorescence images of wild type HH8- (**A**), HH9 (**B-D**), and HH9+ (**E-G**) chick embryos, in whole mount (**A, B, E**) and cross-section (**C-D, F-G**), immunostained for Elavl1 (cyan) and Pax7 (magenta). Dashed white line (**B, E**) indicates level of cross-section (**C-D, F-G**, respectively); dotted white lines outline regions of premigratory and migratory neural crest as indicated. NF, neural folds; NT, neural tube; pNC, premigratory neural crest; mNC, migratory neural crest. Scale bar, 50 μm.

FoxD3 (**Figure 3D**; 61.3 ± 5.5% of the control side, $P = 0.002$, Wilcoxon signed-rank test, $n = 10$ embryos), and *Draxin* (**Figure 3E**; 66.6 ± 1.8% of the control side, $P = 0.03$, Wilcoxon signed-rank test, $n = 6$ embryos) transcripts compared to contralateral control sides. To parse whether this was a specific effect or a broad defect in neural crest development, we also examined additional neural crest genes and found no significant difference in expression between control or Elavl1 knockdown sides for *Pax7* (**Figure 3F**; 87.4 ± 3.1% of the control side, $P = 0.1$, Wilcoxon signed-rank test, $n = 5$ embryos) or *Tfap2b* (**Figure 3G**; 98.2 ± 7.0% of the control side, $P = 0.6$, Wilcoxon signed-rank test, $n = 4$ embryos), indicating a specific defect in a subset of genes required for cranial neural crest specification.

We also performed immunostaining for Pax7 in cross-section to assess if Elavl1 knockdown altered neural crest cell number or dorsal neural tube morphology. Interestingly, the total number of Pax7+ cells was unaffected with Elavl1 knockdown (101.3 ± 4.5% of the control side, $P = 0.6$, one-sample Wilcoxon signed-rank test, $n = 4$ embryos, 11 sections); however we found a significant increase in the number of Pax7+ cells that delaminated from the neural tube (139.4 ± 8.4% of the control side, $P = 0.002$, one-sample Wilcoxon signed-rank test), and concomitant decrease in the number of Pax7+ cells retained within the dorsal neural tube (66.0 ± 5.3% of the control side, $P = 0.001$, one-sample Wilcoxon signed-rank test) (**Figure 3H-I**). To determine what impact premature delamination might have on cranial neural crest migration, we also performed whole mount immunostaining for Pax7 at HH9+ and found significant decrease in cranial neural crest emigration away from the midline (**Figure 3—Supplement 2**; 63.6 ± 4.1% of the control side, $P < 0.001$, Wilcoxon matched-pairs signed rank test, $n = 5$ embryos, 5 measurements per embryo averaged). Taken together, these data suggest that Elavl1 is required during early cranial neural crest development to regulate specification and prevent premature delamination.

Draxin is the primary target of Elavl1 during cranial neural crest specification

To parse the mechanism of Elavl1 function during cranial neural crest specification, we sought to more broadly identify the RNA targets of Elavl1 using bulk RNA-sequencing (RNA-seq) and differential gene expression analysis (**Figure 4A**). Given that Elavl1 is known to bind to and stabilize its RNA targets via 3'-UTR interaction (Chen et al., 2002; Dormoy-Raclet et al., 2007; Katsanou et al., 2009; Rothamel et al., 2021; Shi et al., 2020), we expected expression of potential targets to be reduced with Elavl1 knockdown. Among the differentially expressed genes we identified (**Figure 4—Figure Supplement 1**), 12 were significantly downregulated, with four having established roles in neural crest development and which we validated using HCR—*Axud1*, *Draxin*, *BMP4*, and *Msx1* (**Figure 4B**, **Figure 4—Figure Supplement 1**). We also identified several canonical neural crest genes that were unaffected with Elavl1 knockdown (*e.g. Pax7*, *Tfap2b*, *Snai2*, *Sox9*, and *Zeb2*), consistent with HCR data (**Figure 3**, **Figure 4—Figure Supplement 1**). Together these data suggest Elavl1 does not broadly bind and stabilize the transcripts of neural crest genes, rather it targets specific RNAs to drive cranial neural crest specification.

Notably, *FoxD3* failed to meet our stringency cutoff during RNA-seq analysis due to low expression at the examined stages, and is likely downregulated with Elavl1 knockdown (**Figure 3D**) due to indirect effects from loss of *Axud1* (Simoes-Costa et al., 2015) and therefore unlikely to be a bona fide target of Elavl1. To determine whether Elavl1 directly or indirectly interacts with *Axud1*, *Draxin*, *BMP4*, and *Msx1* mRNAs, we first measured the rate of mRNA decay with actinomycin D treatment to assess the stability of these RNAs, and *Pax7* as a non-target, with or without Elavl1 knockdown (**Figure 4C**); if Elavl1 is required for transcript stability, target RNAs should decay at a faster rate with loss of Elavl1 compared to control. Interestingly, among all the transcripts tested, only *Draxin* had a significant reduction in transcript stability ($P = 0.001$, Mann Whitney test) (**Figure 4D**), suggesting that *Draxin* is the primary target bound and stabilized by Elavl1 during cranial neural crest specification.

To test this hypothesis, we searched the 3'-UTR sequences of *Draxin*, *Axud1*, *BMP4*, *Msx1*, *Pax7*, and *Tfap2b* mRNAs for putative Elavl1 binding sites. The *Draxin* 3'-UTR contained four high probability binding sites, whereas the other 3'-UTRs contained only one (*BMP4*, *Msx1*) or none (*Axud1*, *Pax7*, *Tfap2b*) (**Figure 4—Figure Supplement 2**). Given that Elavl1 contains three RNA recognition motifs (RRMs) that cooperate for RNA recognition (Pabis et al., 2018), it is possible that multiple contacts are required for Elavl1 to bind and stabilize RNAs *in vivo*, and by extension is unlikely for Elavl1 to bind RNAs with only a single putative binding site. Thus, we hypothesize that Elavl1 specifically targets and stabilizes *Draxin* in cranial neural crest through multiple contact sites within its 3'-UTR.

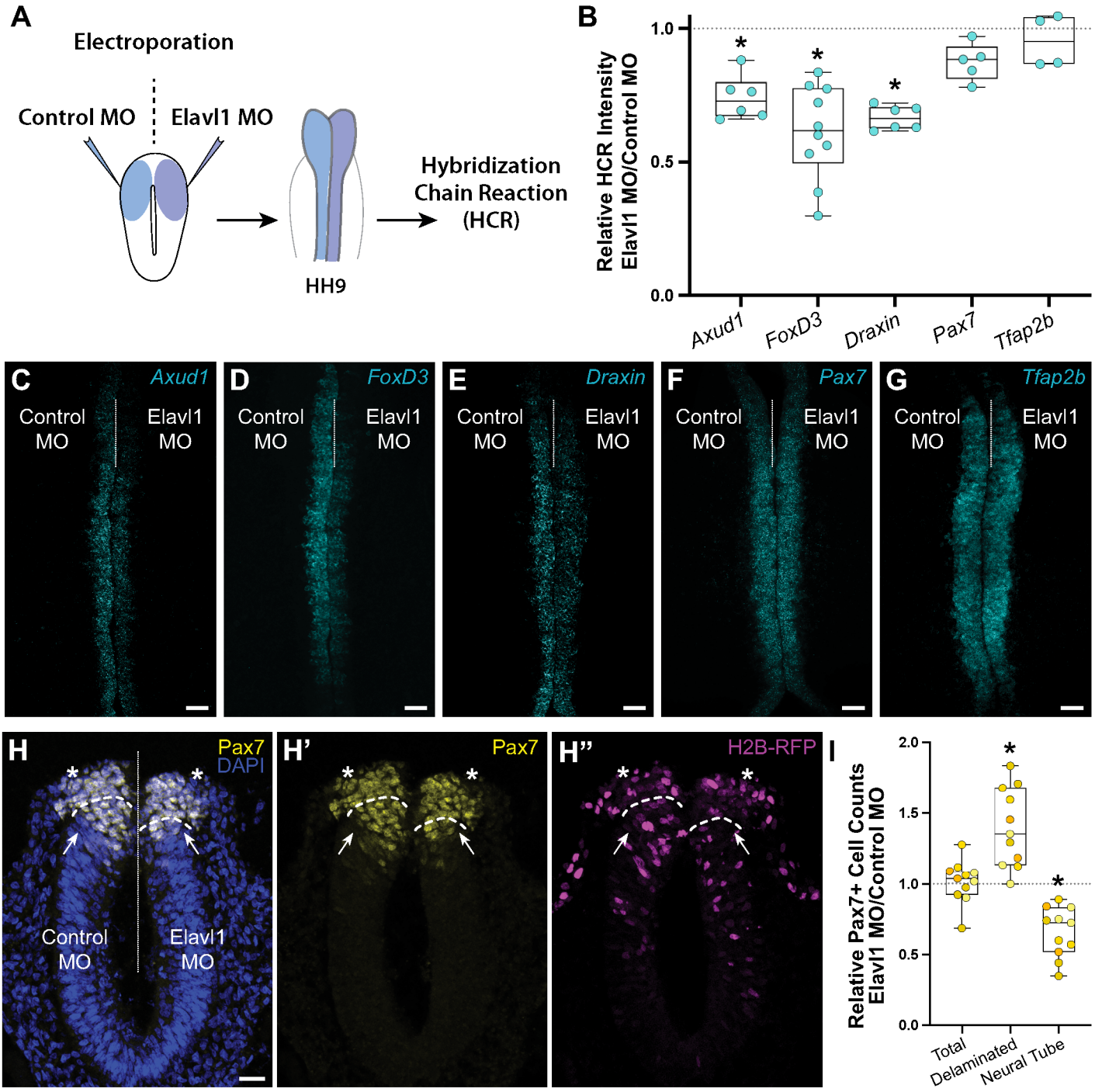

Figure 3. Elavl1 knockdown alters cranial neural crest specification and delamination.
(**A**) Schematic diagram illustrating experimental design. Gastrula stage chick embryos were electroporated bilaterally with a standard control and translation-blocking morpholino (MO) targeting *Elavl1*. Electroporated embryos were subsequently processed for quantitative hybridization chain reaction (HCR) and analyzed in whole mount, comparing the knockdown to the contralateral control side. (**B**) Quantitation of HCR processed embryos for control versus Elavl1 knockdown for cranial neural crest transcripts, calculated as ratio of Elavl1 MO versus control MO integrated density. (**C-G**) Representative confocal maximum intensity projection micrographs for *Axud1* (**C**), *FoxD3* (**D**), *Draxin* (**E**), *Pax7* (**F**), and *Tfap2b* (**G**) transcripts. Dotted white line indicates midline. MO, morpholino. Scale bar, 50 µm. *, $P < 0.05$, Wilcoxon signed-rank test. (**H**) Representative apotome maximum intensity projection micrographs of cross-sectioned embryo bilaterally co-electroporated with a fluorescent electroporation control construct (H2B-RFP) and control MO (left) or Elavl1 MO (right), immunostained for Pax7 (yellow). Nuclei were stained with DAPI (blue). Dotted white line indicates midline. Dashed white lines indicate limit of dorsal neural tube. Arrows indicate "neural tube" Pax7 cells. Asterisks indicate "delaminated" Pax7 cells. Scale bar, 20 µm. (**I**) Quantification of the ratio of Pax7+ cells on Elavl1 MO (right) versus control MO (left) sides of cross-sections. Data are from individual sections; sections from same embryo are displayed in same color ($n = 4$ embryos, 11 sections) *, $P \leq 0.002$, one-sample Wilcoxon signed-rank test. See also **Figure 3—Supplement 1** and **Figure 3—Supplement 2**.

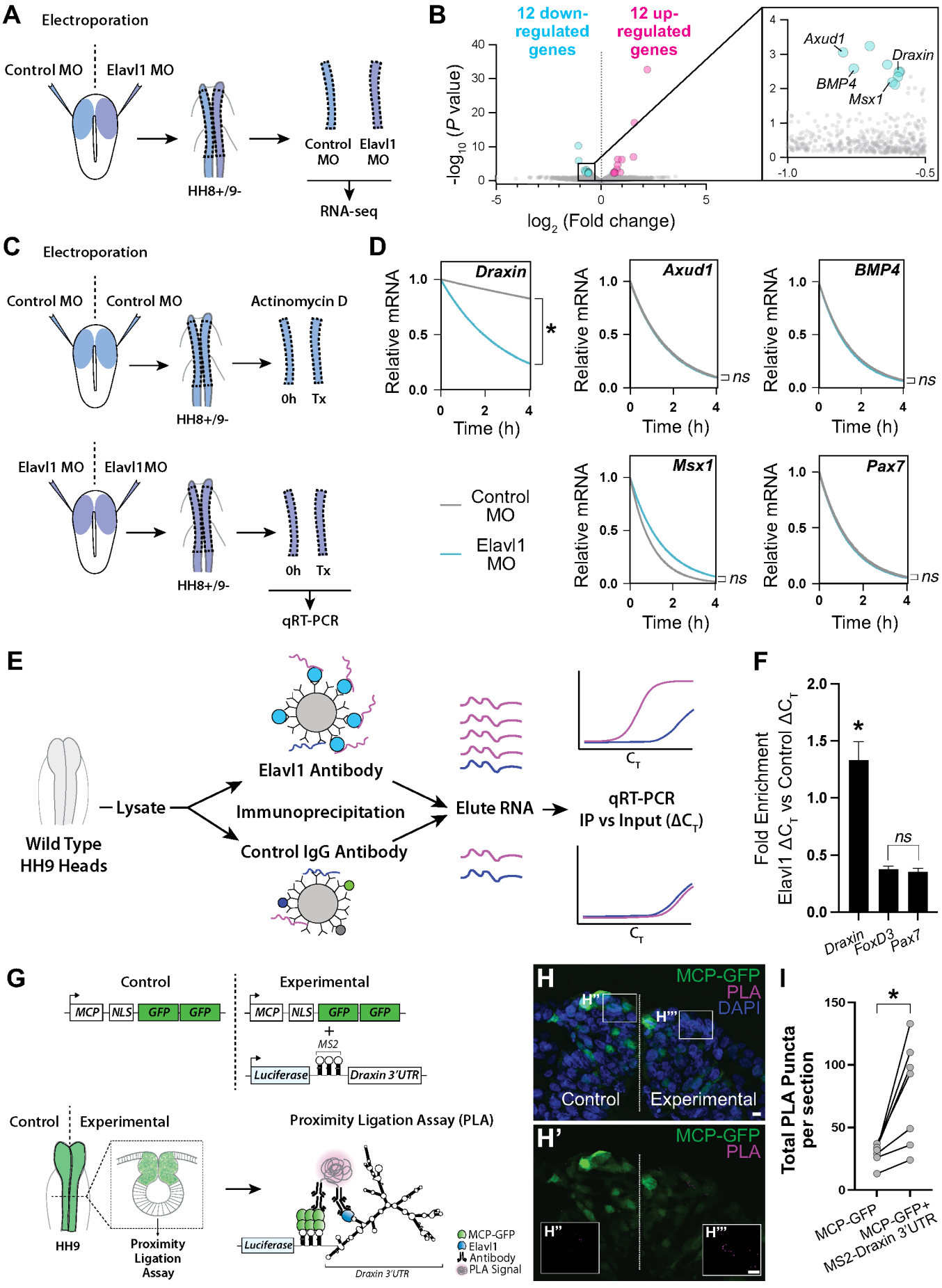

Figure 4. *Draxin* mRNA is the primary target of Elavl1 during cranial neural crest specification.

Figure 4 continued.
(**A**) Schematic diagram illustrating experimental design for RNA-sequencing (RNA-seq). Gastrula stage chick embryos were electroporated bilaterally with a standard control and translation-blocking morpholino (MO) targeting *Elavl1*. Dorsal neural folds were dissected from stage HH8+/9- embryos, pooled (n = 3), and processed for bulk RNA-seq (three biological replicates). (**B**) Volcano plot following differential expression analysis and filtering of RNA-seq data. Of the 24 genes differentially expressed following Elavl1 knockdown (12 upregulated, 12 downregulated), four genes (*Draxin*, *Axud1*, *Msx1*, *BMP4*) have established roles in neural crest development and were significantly downregulated. (**C**) Schematic diagram illustrating experimental design for RNA stability assay. Gastrula stage chick embryos were electroporated bilaterally with control or translation-blocking morpholino (MO) targeting *Elavl1*. Dorsal neural folds were dissected from stage HH8+/9- embryos; left neural folds were used as the 0 hour (h) time point, whereas right neural folds were treated with actinomycin D for 30 min, 2h, or 4h prior to total RNA extraction and qRT-PCR to measure RNA decay. (**D**) Transcript stability plots show *Draxin* mRNA stability is significantly reduced (*, P = 0.001, Mann Whitney test) with Elavl1 knockdown (blue) compared to control (gray), whereas other neural crest mRNAs (*Axud1*, *Msx1*, *BMP4*, *Pax7*) are not (*ns*, non-significant, P = 0.37, Mann Whitney test). (**E**) Schematic illustrating experimental design of RNA-binding protein/RNA co-immunoprecipitation (RIP) to test RNA association with Elavl1 *in vivo* for neural crest targets. Lysates generated from HH9 heads were incubated with antibody-coated beads for Elavl1 or a non-specific IgG to co-immunoprecipitate protein with bound RNAs. In qRT-PCR, specifically bound RNAs would be more abundant and reach threshold before RNAs that were nonspecific, and therefore would have smaller C_T values. C_T, threshold cycle. (**F**) Fold enrichment of RNAs eluted from RIP, quantified by qRT-PCR. *ns*, non-significant, P = 0.89, one-way ANOVA with Tukey's *post hoc* test. *, $P < 0.001$, one-way ANOVA with Tukey's *post hoc* test. Error bars, SEM. (**G**) Schematic diagram illustrating experimental design for Proximity Ligation Assay (PLA). Gastrula stage chick embryos were electroporated bilaterally with a construct expressing a nuclear localized, GFP-tagged MS2 bacteriophage coat protein (MCP-GFP) alone (left) or in combination with a construct containing a Luciferase coding region, MS2 stem loops (which are bound by MCP when transcribed), and the endogenous *Draxin* 3'-untranslated region (MS2-*Draxin* 3'UTR) (right). Following fixation and cross-sectioning at HH9, tissues were incubated with primary antibodies made in goat and rabbit that recognized GFP and Elavl1, respectively. Secondary antibodies against goat and rabbit IgG were labeled with complementary oligonucleotides that generate a fluorescent signal due to rolling circle amplification only when in close proximity (<40nm). Thus, fluorescence signal (magenta) would indicate *in vivo* interaction between MCP-GFP and endogenous Elavl1. (**H**) Representative confocal maximum intensity projection micrograph of dorsal neural folds from cross-sectioned HH9 embryo bilaterally electroporated with MCP-GFP (green) alone ("control", left) or with MS2-*Draxin* 3'-UTR ("experimental", right), processed for PLA (magenta) as illustrated in panel (**G**), and stained for DAPI (blue). Boxes in (**H**) indicate zoomed-in areas in (**H''**) and (**H'''**). Scale bar, 5 µm. (**I**) Quantitation of total number of PLA puncta per section for (n = 3 embryos, 2 sections/embryo). *, P = 0.016, two-tailed Wilcoxon matched-pairs signed rank test. See also **Figure 4—Supplement 1** and **Figure 4—Supplement 2**.

To confirm that *Draxin* mRNA is bound by Elavl1 *in vivo*, we first performed an RNA immunoprecipitation (RIP) followed by quantitative reverse transcription-PCR (qRT-PCR) to pull down endogenous Elavl1 ribonucleoprotein (RNP) complexes. To this end, we incubated lysate generated from wild type HH9 embryonic heads with magnetic beads coated with either Elavl1 antibody or a rabbit IgG non-specific control antibody, then eluted bound RNA and performed qRT-PCR, comparing immunoprecipitated RNAs ("IP") with RNAs extracted from a fraction of the input lysate ("Input"). We expected that RNAs bound by Elavl1 would be enriched in the IP compared to the Input, whereas non-specifically associated RNAs, *i.e.* non-targets, would not (**Figure 4E**). We found that *Pax7* and *FoxD3* mRNAs (non-targets) were neither enriched in the IP, nor significantly different from each other (P = 0.89, one-way ANOVA with Tukey's *post hoc* test); however, *Draxin* mRNA was significantly enriched with Elavl1 IP compared to *Pax7* and *FoxD3* ($P < 0.001$, one-way ANOVA with Tukey's *post hoc* test) (**Figure 4F**), suggesting that Elavl1 specifically associated with endogenous *Draxin* mRNA. However, this assay could not distinguish whether *Draxin* was bound directly or indirectly, or where within the transcript it might be associating with Elavl1.

To test whether *Draxin* was directly bound by Elavl1 within the 3'-UTR, we performed a proximity ligation assay (PLA), wherein *in situ* fluorescent signal can be detected as puncta only when two proteins are in close proximity (<40nm), indicating a direct interaction in vivo. Taking advantage of the MS2-MCP reporter system (Tutucci et al., 2018), we electroporated a construct encoding a GFP-tagged MS2 bacteriophage coat protein (MCP-GFP) alone ("Control") or in combination with ("Experimental") a construct containing a Luciferase coding region, MS2 stem loops (bound by MCP when transcribed), and the endogenous *Draxin* 3'-untranslated region (MS2-*Draxin* 3'UTR) and performed PLA with antibodies against Elavl1 and GFP (**Figure 4G**). We observed significantly more PLA puncta with expression of MS2-*Draxin* 3'UTR (**Figure 4H-I**), indicating a specific and direct interaction between Elavl1 and the *Draxin* 3'-UTR.

Elavl1 maintains cranial neural crest specification via *Draxin* mRNA stabilization

Our data suggest that Elavl1 specifically binds and stabilizes *Draxin* mRNA as its primary target during cranial neural crest specification. To determine if defects in cranial neural crest specification with Elavl1 knockdown were indirect, and due to *Draxin* downregulation, we examined *FoxD3*, *Axud1*,

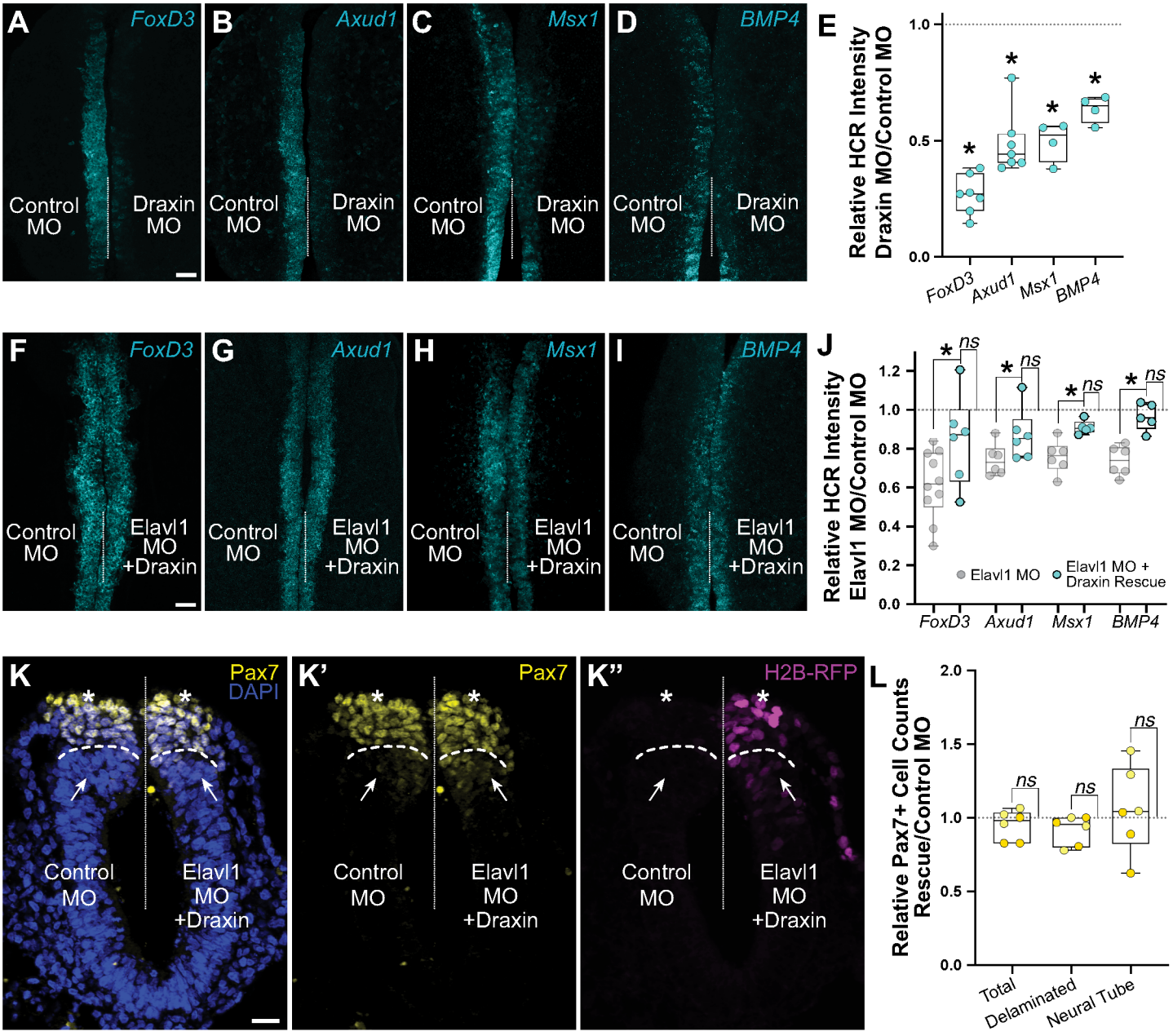

Figure 5. Elavl1 knockdown phenotypes are rescued by *Draxin*.
(**A-D**) Representative confocal maximum intensity projection micrographs of HCR processed embryos for *FoxD3* (**A**), *Axud1* (**B**), *Msx1* (**C**), and *BMP4* (**D**) transcripts in whole mount embryos bilaterally electroporated with control morpholino (left) or Draxin morpholino (right). Dotted white line indicates midline. MO, morpholino. Scale bar, 50 µm. (**E**) Quantitation of HCR processed embryos for control versus Elavl1 knockdown, calculated as ratio of Elavl1 MO versus control MO integrated density. *, $P < 0.02$, Wilcoxon matched-pairs signed rank or paired *t*-test as indicated in text. (**F-I**) Representative confocal maximum intensity projection micrographs of HCR processed embryos for *FoxD3* (**F**), *Axud1* (**G**), *Msx1* (**H**), and *BMP4* (**I**) transcripts in whole mount embryos bilaterally electroporated with control morpholino (left) or Elavl1 morpholino and a *Draxin* overexpression construct (right). Dotted white line indicates midline. MO, morpholino. Scale bar, 50 µm. (**J**) Quantitation of HCR processed embryos for control versus Elavl1 knockdown with *Draxin* rescue, calculated as ratio of Elavl1 MO + Draxin versus control MO integrated density. *ns*, non-significant, $P > 0.09$, Wilcoxon signed-rank test. Grayed values indicating Elavl1 MO data were originally presented in Figure 3 and are reproduced here to illustrate rescue. *, $P < 0.05$, one-tailed paired *t*-test. (**K**) Representative apotome maximum intensity projection micrographs of cross-sectioned embryo bilaterally electroporated with control MO (left) or Elavl1 MO + Draxin overexpression (right), immunostained for Pax7 (yellow). *Draxin* overexpression is indicated by expression of H2B-RFP (magenta). Nuclei were stained with DAPI (blue). Dotted white line indicates midline. Dashed white lines indicate limit of dorsal neural tube. Arrows indicate "neural tube" Pax7 cells. Asterisks indicate "delaminated" Pax7 cells. Scale bar, 20 µm. (**L**) Quantification of the ratio of Pax7+ cells on Elavl1 MO + Draxin (right, "Rescue") versus control MO (left) sides of cross-sections. Data are from individual sections; sections from same embryo are displayed in same color ($n = 3$ embryos, 6 sections). *ns*, non-significant, $P > 0.12$, one-sample Wilcoxon signed-rank test.

Msx1, and *BMP4* expression in Draxin knockdown embryos. We electroporated control and Draxin MO (Hutchins and Bronner, 2018, 2019) bilaterally, and performed HCR at HH9. As with Elavl1 MO (**Figure 3**), we observed significant reduction in the levels of *FoxD3* (**Figure 5A**; 26.8 ± 3.2% of the control side, $P < 0.02$, Wilcoxon matched-pairs signed rank, $n = 7$ embryos), *Axud1* (**Figure 5B**; 48.8 ± 5.1% of the control side, $P < 0.01$, paired *t*-test, $n = 7$ embryos), *Msx1* (**Figure 5C**; 49.7 ± 5.8% of the control side, $P < 0.01$, paired *t*-test, $n = 4$ embryos), and *BMP4* (**Figure 5D**; 63.6 ± 4.0% of the control side, $P < 0.01$, paired *t*-test, $n = 4$ embryos) transcripts compared to contralateral control sides (**Figure 5E**).

We next asked whether *Draxin* upregulation alone was sufficient to rescue the Elavl1 MO phenotype (**Figure 3B-E**). To this end, we co-electroporated Elavl1 MO with a *Draxin* overexpression construct [Draxin-FLAG; (Hutchins and Bronner, 2018, 2019)], and assessed neural crest specification with HCR. Indeed, exogenous *Draxin* was sufficient to significantly restore *FoxD3* (**Figure 5F**; 84.5 ± 9.6% of the control side, $n = 6$ embryos), *Axud1* (**Figure 5G**; 90.3 ± 5.0% of the control side, $n = 6$ embryos), *Msx1* (**Figure 5H**; 91.0 ± 1.5% of the control side, $n = 5$ embryos), and *BMP4* (**Figure 5I**; 96.5 ± 3.1% of the control side, $n = 5$ embryos) expression from Elavl1 knockdown ($P < 0.05$, one-tailed paired *t*-test) to expression levels not significantly different from control (**Figure 5J**; $P > 0.09$, Wilcoxon signed-rank test). To determine if exogenous *Draxin* was sufficient to rescue the premature delamination phenotype (**Figure 3H-I**) caused by Elavl1 knockdown, we also performed immunostaining for Pax7 in cross-section to assess neural crest cell number and dorsal neural tube morphology. Indeed, co-electroporation of Draxin-FLAG with Elavl1 MO was able to rescue the number of Pax7+ cells that delaminated and remained within the dorsal neural tube to near-control levels (**Figure 5L**; 91.6 ± 4.0% and 105.8 ± 12.0% of the control side, respectively, $n = 3$ embryos, 6 sections, $P > 0.12$, one-sample Wilcoxon signed-rank test). Taken together, these data indicate that *Draxin* mRNA is the primary target of Elavl1 in premigratory cranial neural crest and is stabilized via 3'-UTR interaction to maintain neural crest specification.

DISCUSSION

Understanding of neural crest development has been greatly enhanced by the identification of key transcriptional circuits that control its developmental progression. Recent studies suggest a critical role for post-transcriptional regulation in the refinement of the expression outputs of these GRNs. Here, we identified and characterized Elavl1 as an RNA-binding protein essential for the maintenance of cranial neural crest specification via its stabilization of the Wnt antagonist *Draxin*. We found that loss of Elavl1, and by extension its target, *Draxin*, interferes with output from multiple nodes of the GRNs required for neural crest specification, including those driven by Wnt and BMP (Hovland et al., 2020; Simoes-Costa et al., 2015; Tribulo et al., 2003). Together, our data implicate Elavl1 as a point of integration to coordinate signaling from parallel but independent GRNs.

At a mechanistic level, our study is consistent with previous work examining Elavl1 function in other cellular contexts, with respect to its role as a stabilizing RNA-binding protein via 3'-UTR interaction (Chen et al., 2002; Dormoy-Raclet et al., 2007; Katsanou et al., 2009; Rothamel et al., 2021; Shi et al., 2020). In the context of embryonic development, our study aligns well with data from knockout mouse consistent with an important role for Elavl1 in intersecting signaling cascades; interestingly, this prior work similarly observed indirect downregulation of *BMP4* with loss of Elavl1, though an upstream mediator remained unidentified (Katsanou et al., 2009). In neural crest specification, we identified a single biologically relevant target of Elavl1, whereas prior high-throughput studies found many RNAs directly bound by Elavl1 (Mukherjee et al., 2011; Rothamel et al., 2021). Whether this is a feature specific to neural crest is unclear, though the knockout mouse work suggests that during embryonic development Elavl1 function and RNA targets are driven by spatiotemporal determinants (Katsanou et al., 2009), which may be due ribonucleoprotein complex heterogeneity as a result of tissue-specific expression of other interacting RNA-binding proteins. Taken in the context of these prior studies, we speculate that despite broad tissue expression of Elavl1 across embryonic development, specificity in neural crest is achieved through spatiotemporally-regulated combinatorial expression of post-transcriptional regulators and RNA regulons (Keene, 2007; Keene and Tenenbaum, 2002).

It is important to note that, while Elavl1 expression persists in cranial neural crest during the initiation of EMT and migration, *Draxin* must be rapidly downregulated for these processes to proceed (Hutchins and Bronner, 2018, 2019; Hutchins et al., 2021). Thus, we hypothesize that Elavl1 becomes endogenously displaced from *Draxin* at the onset of EMT, though it is yet unclear how this is achieved. RNA-binding proteins are known to alter association with targets due to post-translational modifications such as phosphor-

ylation or alternative RNA-binding protein competition (Dassi, 2017; Garcia-Maurino et al., 2017; Liu et al., 2015). Indeed, inhibition of serine-threonine kinases has been shown in neural crest to increase cell-cell adhesions and negatively impact cell migration (Monier-Gavelle and Duband, 1995), suggesting kinase-driven signaling pathway activation coincident with neural crest EMT; this is interesting given established roles for serine-threonine phosphorylation in modulating Elavl1 RNA-binding activity and target selection (Grammatikakis et al., 2017). Thus, we speculate that Elavl1 serine-threonine phosphorylation, either in combination with or as an alternative to competitive RNA-binding protein displacement, likely facilitates *Draxin* release and turnover at the onset of EMT.

Because its primary target during specification is downregulated while Elavl1 expression persists, this suggests there are likely additional targets and roles for Elavl1 beyond *Draxin* stabilization. Elavl1 has been shown in other contexts to stabilize *Snail1* (Dong et al., 2007) and *matrix metalloprotease-9* (*MMP-9*) (Yuan et al., 2011), factors with well-established roles in neural crest EMT (Cano et al., 2000; Kalev-Altman et al., 2020; Monsonego-Ornan et al., 2012; Strobl-Mazzulla and Bronner, 2012; Taneyhill et al., 2007). Given that the neural crest specification GRNs is proceeded by activation of an EMT GRN also coinciding with Elavl1 expression, we speculate that Elavl1 likely intersects with additional GRNs following specification. It is possible one or more of the downregulated genes we identified through RNA-seq that were not important for specification may yet be targets of Elavl1, with functions later in neural crest development. To fully understand how Elavl1 exerts control over key developmental processes, these possibilities will need to be explored.

MATERIALS AND METHODS

Model organism and embryo collection

Fertile chicken eggs (*Gallus gallus*) were purchased locally (Sun State Ranch, Monrovia, CA), and incubated in a humidified 37ºC incubator to the specified Hamburger-Hamilton (HH) stage (Hamburger and Hamilton, 1951). Live embryos were removed from eggs with Whatman filter paper as described (Hutchins and Bronner, 2018, 2019) and stored in Ringer's solution until further processing.

Immunohistochemistry and Hybridization Chain Reaction

For whole mount immunohistochemistry, embryos were fixed at room temperature for 20 min with 4% paraformaldehyde in sodium phosphate buffer. For cross-sections, embryos were fixed at room temperature for 1 h, then washed, embedded, and cryosectioned as described (Hutchins and Bronner, 2018, 2019) prior to immunohistochemistry. Washes, blocking (10% donkey serum), and antibody incubations were performed in TBSTx (0.5 M Tris-HCl/1.5 M NaCl/10 mM $CaCl_2$/0.5% Triton X-100/0.001% Thimerosal) as described (Chacon and Rogers, 2019; Manohar et al., 2020). Primary antibodies are listed in the Key Resources Table. Species-specific secondary antibodies were labeled with Alexa Fluor 568 and 647 (Invitrogen) and used at 1:1000 or 1:500, respectively. For nuclear staining on cross-sections, DAPI (4',6-Diamidino-2-Phenylindole) was added to the secondary antibody solution at [14.3 µM] final concentration. Coverslips were mounted using Fluoromount-G (SouthernBiotech).

Hybridization Chain Reaction (HCR) was performed as described (Gandhi et al., 2020). Embryos were fixed at room temperature for 1 h with 4% paraformaldehyde in phosphate buffered saline (PBS) prior to HCR processing. Custom HCR probes were designed and ordered through Molecular Technologies.

Gene expression constructs and perturbation

Translation-blocking antisense morpholino oligo (MO) for *Elavl1* (Gene Tools; Key Resources Table) was designed to span the *Elavl1* (GenBank: NM_204833.1) start codon from nucleotide –20 to +5, and electroporated at [2 mM]. Draxin MO was described previously (Hutchins and Bronner, 2018, 2019), and electroporated at [1 mM]. The standard control MO (Gene Tools) was used for contralateral control electroporation. MOs were co-electroporated with pCIG (Megason and McMahon, 2002) or pCI-H2B-RFP (Betancur et al., 2010) to increase electroporation efficiency and to visualize successfully electroporated cells. The Draxin-FLAG overexpression construct (Draxin OE) (Hutchins and Bronner, 2018, 2019) and the MCP-GFP construct (Hutchins et al., 2020) have been previously described. The MS2-*Draxin* 3'UTR construct used in this study was generated by exchanging the mTurq2 coding region for a Luciferase coding region in a previously described MS2-*Draxin* 3'UTR construct (Hutchins et al., 2020). Electroporations were performed on HH4 gastrula stage chicken embryos as described previously (Hutchins and Bronner, 2018, 2019).

RNA-sequencing and data analysis

For single cell RNA-seq analysis, raw data from

(Williams et al., 2019) were downloaded from Gene Expression Omnibus (GEO; GSE130500) and processed for quality assessment using FastQC (Andrews, 2014). The reads were trimmed and filtered using Cutadapt (Martin, 2011), following which they were aligned to the chicken galgal6 (GRCg6a) genome assembly using Bowtie2 (Langmead and Salzberg, 2012). The alignment files generated were used to count features using HTSeq-Count (Anders et al., 2015). All further analyses were performed in R using Seurat (Butler et al., 2018) as previously described (Gandhi et al., 2020). Gene Ontology terms associated with all genes in the chicken genome were identified using the biomaRt package (Durinck et al., 2009). This dataset was queried for the ontology terms expected to be associated with RNA-Binding Proteins, such as "binds mRNA," "binds 3' UTR," "regulates translation," and "stabilizes RNA." All feature plots and strip plots were made using Seurat.

For bulk RNA-sequencing, dorsal neural folds from morpholino-electroporated embryos grown to stage HH8+/9- were dissected in DEPC-treated PBS and pooled (n = 3) before total RNA was extracted using an RNAqueous™-Micro kit (Thermo). cDNA libraries (three biological replicates per treatment) were prepared from 10 ng total RNA per pooled sample using the Takara Bio SMART-Seq v4 Ultra Low Input cDNA kit, according to manufacturer instructions. Single-end RNA-Sequencing was performed at the Caltech Millard and Muriel Jacobs Genetics and Genomics Laboratory at a depth of 20 million reads. Reads were processed and differential expression analysis was performed as described (Hutchins et al., 2021; Piacentino et al., 2021). We subsequently filtered the gene lists to exclude lowly expressed genes (average normalized count values < 250), resulting in a filtered list of 24 differentially expressed genes (12 downregulated, 12 upregulated) with greater than 1.5 fold change and $P < 0.05$ cutoff.

RNA decay assay

Embryos were electroporated bilaterally with either control MO or Elavl1 MO and grown to HH8+/9-. Dorsal neural folds were dissected in DEPC-treated PBS, pooled (n = 3), and suspended in explant culture media (DMEM supplemented with 10% Fetal Bovine Serum, 10% Chick Embryo Extract, and 1% Penicillin/Streptomycin). Actinomycin D [10 µg/mL] or DMSO alone (for 0h time point) was added to neural fold samples, which were then incubated at 37°C/5% CO_2 for 0h, 30min, 2h, or 4h. Following the specified incubation time, neural fold samples were centrifuged at 300 xg for 3 min to remove media then washed three times with DEPC-treated PBS.

Total RNA was then extracted using the RNAqueousTM-Micro kit (Thermo) and 50 ng of RNA was reverse transcribed using SuperScript III and oligo dT priming. Following reverse transcription, we performed qPCR using FastStart Universal SYBR Green Master (Rox) with cDNA (diluted 1:10) and gene-specific primers (**Key Resources Table**) on a QuantStudio 3 Real-Time PCR System (Applied Biosystems) in triplicate. Average C_T values were calculated for 0h time points. Individual C_T values for 30 min, 2h, and 4h actinomycin D time points were subtracted from the 0h average C_T, and fold change was calculated for each technical replicate from the start of transcription inhibition (t=0h) to each actinomycin D time point for each target. RNA decay rates were calculated and plotted using one phase decay in Prism9 (n = three biological replicates).

RNA immunoprecipitation (RIP) and qRT-PCR

RNA immunoprecipitation (RIP) was performed as described (Hutchins and Szaro, 2013; Jayaseelan et al., 2014), with minor modifications. Briefly, Protein-G Dynabeads were washed with NT-2 (50 mM Tris-HCl, 150 mM NaCl, 1 mM $MgCl_2$, 0.05% NP-40), blocked in NT-2/5% BSA for 1 h at room temperature, then incubated with 5 µg antibody (Elavl1 IgG or Control IgG) in NT-2/5% BSA for 1 h at room temperature. Following antibody incubation, antibody-coated beads were washed with NT-2 and resuspended in NET-2 (NT-2, 20 mM EDTA, 400 U RNaseOUT, 1x cOmplete, Mini EDTA-free Protease Inhibitor) until addition of cleared lysate.

Embryonic heads were dissected in Ringer's solution, washed in RNase-free PBS, and dissociated in Accumax (Innovative Cell Technologies) for 15 min at room temperature. Following dissociation, cells were pelleted at 2000 xg for 4 min at 4ºC, washed in RNase-free PBS, and resuspended in Polysome Lysis Buffer (0.1 M KCl, 5 mM $MgCl_2$, 10 mM HEPES, 0.5% NP-40, 200 U RNaseOUT, 1x cOmplete, Mini EDTA-free Protease Inhibitor). Cells were frozen at -80ºC overnight to complete lysis and reduce adventitious binding. Lysate was then thawed on ice, vortexed, and centrifuged at 14,000 xg for 10 min at 4ºC to remove cellular debris, then cleared lysate was added to antibody-coated beads in NET-2. Immediately following addition of cleared lysate, 10% was removed to serve as an Input control. IP reaction was tumbled at room temperature for 1 h, beads were then washed in NT-2, and RNA was eluted in Proteinase K Buffer (NT-2, 1% SDS, 1.2 mg/mL Proteinase K) for 30 min at 55ºC and phenol/chloroform

extracted.

RNA from Input and IP samples was reverse transcribed using SuperScript III and oligo dT priming. Following reverse transcription, we performed qPCR using FastStart Universal SYBR Green Master (Rox) with cDNA (diluted 1:5) and gene-specific primers (**Key Resources Table**) on a QuantStudio 3 Real-Time PCR System (Applied Biosystems) in triplicate. We determined ΔC_T (ΔC_T = Input C_T – IP C_T) for *Draxin*, *FoxD3*, and *Pax7* for Elavl1 and Control IgG RIP samples, then calculated fold enrichment values (= $2^{(\text{Average Control IgG } \Delta C_T - \text{Elavl1 } \Delta C_T)}$) for each target and replicate.

Proximity Ligation Assay

Embryos were electroporated bilaterally with MCP-GFP alone ("control"), or MCP-GFP and MS2-Draxin 3'UTR ("experimental"), grown to stage HH9, then fixed at room temperature for 1 h, washed, embedded, and cryosectioned as described (Hutchins and Bronner, 2018, 2019). Sections were processed using a DuoLink PLA kit (Millipore/Sigma) with Anti-Rabbit MINUS PLA probe, anti-Goat PLUS PLA probe, and Far Red PLA detection reagent, and primary antibodies for Elavl1 and GFP, according to the manufacturer's DuoLink PLA Fluorescence protocol.

Image acquisition and analysis

Confocal images were acquired using an upright Zeiss LSM 880 at the Caltech Biological Imaging Facility, and epifluorescence images were acquired using a Zeiss Imager.M2 with an ApoTome.2 module. Images were minimally processed for brightness/contrast and pseudocolored using Fiji (ImageJ, NIH) and Adobe Photoshop.

Relative fluorescence intensity was determined in Fiji. For each whole mount image, the line tool was used to draw an ROI surrounding the area of neural crest indicated by positive HCR fluorescence for the genes examined. For cross-sections, ROIs were drawn surrounding the neural crest and neural tube based on tissue morphology from nuclear staining. Following background subtraction (50-pixel rolling ball radius), integrated density was quantified for the ROIs on the control electroporated (left) and experimental electroporated (right) sides from the same embryo. Relative fluorescence intensity was then calculated by dividing the integrated density measurements for the experimental versus the control side of the same embryo.

Pax7 cell counts were performed as described (Hutchins and Bronner, 2018). The limit of the dorsal neural tube and characterization of cells as "delaminated" or "neural tube" was determined based on tissue morphology from nuclear staining. For relative migration distance determined from Pax7-stained embryos, distance of migration was measured in Fiji as described (Hutchins and Bronner, 2018).

For Proximity Ligation Assay (PLA) analysis, confocal micrographs were processed in Fiji. Following background subtraction (50-pixel rolling ball radius), ROIs were drawn surrounding the neural crest and neural tube based on tissue morphology from nuclear staining, then puncta (PLA signal) were counted using "analyze particles" function following global manual thresholding to reduce the appearance of nonspecific puncta outside of electroporated regions.

Cloning of the Gallus Axud1 3'-untranslated region (3'-UTR)

Given that the 3'-UTR sequence of Gallus Axud1 was not available in a public repository, to determine whether the Axud1 3'-UTR contained potential Elavl1 binding sites, we performed 3'-Rapid Amplification of cDNA Ends (3'RACE) as described (Scotto-Lavino et al., 2006). Briefly, reverse transcription was performed using the Q_T primer on total RNA extracted from HH8-9 embryos. First round PCR was performed on Q_T-primed cDNA using the Q_O primer and *Axud1* Gene Specific Primer 1. Second round PCR was then performed on this amplification product using the Q_I primer and *Axud1* Gene Specific Primer 2. The resulting PCR product was cloned into the pGEM-T Easy vector (Promega) and eight of these clones were sequenced, and the consensus 3'-UTR sequence deposited to GenBank (Accession # ON920861). Primer sequences can be found in the **Key Resources Table**.

RNA structure and Elavl1 binding site prediction

Secondary structures for the *Draxin* 3'-UTR (GenBank: AB427147.1), *Axud1* 3'-UTR (GenBank: ON920861), *Msx1* 3'-UTR (Ensembl: ENSGALT00000024209.4), *BMP4* 3'-UTR (Ensembl: ENSGALT00000020316.7), *Pax7* 3'-UTR (Ensembl: ENSGALT00000048594.2), and *Tfap2b* 3'-UTR (Ensembl: ENSGALT00000026916.6) were predicted using 'mfold' web server with default settings (Zuker, 2003). Elavl1 binding sites were predicted using RBPDB (Cook et al., 2011) with 0.9 threshold.

Statistical analyses

Statistical analyses were performed using Prism (8, 9; GraphPad Software). *P* values are defined in the text, and significance was established with

$P < 0.05$. *P* values were calculated using Wilcoxon signed-rank, Mann Whitney, one-sample *t*-tests, one-way ANOVA with *post-hoc* Tukey, unpaired or paired *t*-tests as indicated; tests were two-tailed unless otherwise specified in the text/legend. Data were confirmed to be normally distributed using Kolmogorov-Smirnov or Kruskal-Wallis tests for parametric tests. Data measuring fluorescence intensities or cell counts for Experimental/Control sides are presented as box plots with individual data points shown. Bar graphs representing qPCR fold enrichment are presented as mean values, with error bars indicating SEM. Number of embryos and replicates are indicated in figure legends and/or text. Post hoc power analyses (Faul et al., 2007) confirmed sufficient statistical power was reached (≥0.8) for reported *P* values and sample sizes.

ACKNOWLEDGMENTS

We thank A. Collazo and G. Spigolon for imaging assistance at the Caltech Biological Imaging Facility; M. Schwarzkopf and G. Shin (Molecular Technologies) for HCR probe design; I. Antoshechkin of the Caltech Millard and Muriel Jacobs Genetics and Genomics Laboratory for sequencing of RNA-seq libraries; S. Manohar for assistance with *Axud1* 3'-RACE; and G. da Silva Pescador and R. Galton for assistance with pilot experiments.

FUNDING

This work was supported by the National Institutes of Health [R01DE027538 and R01DE027568 to M.E.B; K99DE028592 to E.J.H; K99DE029240 to M.L.P.], the California State University—Northridge BUILD PODER program [TL4GM118977], and the Amgen Foundation Caltech Amgen Scholars Program [J.C.].

COMPETING INTERESTS

The authors declare no competing interests.

DATA AVAILABILITY

RNA-sequencing datasets have been deposited on NCBI under the accession number PRJNA861325. The 3' untranslated region (UTR) sequence for *Axud1* has been deposited to GenBank under accession number ON920861.

REFERENCES

Abdelmohsen, K., Gorospe, M., 2010. Posttranscriptional regulation of cancer traits by HuR. Wiley Interdiscip Rev RNA 1, 214-229.

Anders, S., Pyl, P.T., Huber, W., 2015. HTSeq--a Python framework to work with high-throughput sequencing data. Bioinformatics 31, 166-169.

Andrews, S., 2014. FastQC A Quality Control tool for High Throughput Sequence Data. http://www.bioinformatics.babraham.ac.uk/projects/fastqc/.

Betancur, P., Bronner-Fraser, M., Sauka-Spengler, T., 2010. Genomic code for Sox10 activation reveals a key regulatory enhancer for cranial neural crest. Proceedings of the National Academy of Sciences of the United States of America 107, 3570-3575.

Bhattacharya, D., Rothstein, M., Azambuja, A.P., Simoes-Costa, M., 2018. Control of neural crest multipotency by Wnt signaling and the Lin28/let-7 axis. Elife 7.

Butler, A., Hoffman, P., Smibert, P., Papalexi, E., Satija, R., 2018. Integrating single-cell transcriptomic data across different conditions, technologies, and species. Nature biotechnology 36, 411-420.

Cano, A., Perez-Moreno, M.A., Rodrigo, I., Locascio, A., Blanco, M.J., del Barrio, M.G., Portillo, F., Nieto, M.A., 2000. The transcription factor snail controls epithelial-mesenchymal transitions by repressing E-cadherin expression. Nature cell biology 2, 76-83.

Chacon, J., Rogers, C.D., 2019. Early expression of Tubulin Beta-III in avian cranial neural crest cells. Gene expression patterns : GEP 34, 119067.

Chen, C.Y., Xu, N., Shyu, A.B., 2002. Highly selective actions of HuR in antagonizing AU-rich element-mediated mRNA destabilization. Molecular and cellular biology 22, 7268-7278.

Cibi, D.M., Mia, M.M., Guna Shekeran, S., Yun, L.S., Sandireddy, R., Gupta, P., Hota, M., Sun, L., Ghosh, S., Singh, M.K., 2019. Neural crest-specific deletion of Rbfox2 in mice leads to craniofacial abnormalities including cleft palate. eLife 8, e45418.

Cook, K.B., Kazan, H., Zuberi, K., Morris, Q., Hughes, T.R., 2011. RBPDB: a database of RNA-binding specificities. Nucleic acids research 39, D301-308.

Copeland, J., Simoes-Costa, M., 2020. Post-transcriptional tuning of FGF signaling mediates neural crest induction. Proceedings of the National Academy of Sciences 117, 33305-33316.

Dassi, E., 2017. Handshakes and Fights: The Regulatory Interplay of RNA-Binding Proteins. Front Mol Biosci 4, 67.

Dennison, B.J.C., Larson, E.D., Fu, R., Mo, J., Fantauzzo, K.A., 2021. Srsf3 mediates alternative RNA splicing downstream of PDGFRalpha signaling in the facial mesenchyme. Development 148.

Dong, R., Lu, J.G., Wang, Q., He, X.L., Chu, Y.K., Ma, Q.J., 2007. Stabilization of Snail by HuR in the process of hydrogen peroxide induced cell migration. Biochem Biophys Res Commun 356, 318-321.

Dormoy-Raclet, V., Menard, I., Clair, E., Kurban, G., Mazroui, R., Di Marco, S., von Roretz, C., Pause, A., Gallouzi, I.E., 2007. The RNA-binding protein HuR promotes cell migration and cell invasion by stabilizing the beta-actin mRNA in a U-rich-element-dependent manner. Molecular and cellular biology 27, 5365-5380.

Durinck, S., Spellman, P.T., Birney, E., Huber, W., 2009. Mapping identifiers for the integration of genomic datasets with the R/Bioconductor package biomaRt. Nature protocols 4, 1184-1191.

Faul, F., Erdfelder, E., Lang, A.G., Buchner, A., 2007. G*Power 3: a flexible statistical power analysis program for the social, behavioral, and biomedical sciences. Behav Res Methods 39, 175-191.

Forman, T.E., Dennison, B.J.C., Fantauzzo, K.A., 2021. The Role of RNA-Binding Proteins in Vertebrate Neural Crest and Craniofacial Development. J Dev Biol 9.

Gandhi, S., Bronner, M.E., 2018. Insights into neural crest development from studies of avian embryos. The International journal of developmental biology 62, 183-194.

Gandhi, S., Hutchins, E.J., Maruszko, K., Park, J.H., Thomson, M., Bronner, M.E., 2020. Bimodal function of chromatin remodeler Hmga1 in neural crest induction and Wnt-dependent emigration. Elife 9.

Garcia-Maurino, S.M., Rivero-Rodriguez, F., Velazquez-Cruz, A., Hernandez-Vellisca, M., Diaz-Quintana, A., De la Rosa, M.A., Diaz-Moreno, I., 2017. RNA Binding Protein Regulation and Cross-Talk in the Control

of AU-rich mRNA Fate. Front Mol Biosci 4, 71.

Gou, Y., Zhang, T., Xu†, J., 2015. Transcription Factors in Craniofacial Development: From Receptor Signaling to Transcriptional and Epigenetic Regulation. Current Topics in Developmental Biology.

Grammatikakis, I., Abdelmohsen, K., Gorospe, M., 2017. Posttranslational control of HuR function. Wiley Interdiscip Rev RNA 8.

Hamburger, V., Hamilton, H.L., 1951. A series of normal stages in the development of the chick embryo. J Morphol 88, 49-92.

Hovland, A.S., Rothstein, M., Simoes-Costa, M., 2020. Network architecture and regulatory logic in neural crest development. Wiley Interdiscip Rev Syst Biol Med 12, e1468.

Hutchins, E.J., Bronner, M.E., 2018. Draxin acts as a molecular rheostat of canonical Wnt signaling to control cranial neural crest EMT. The Journal of cell biology 217, 3683-3697.

Hutchins, E.J., Bronner, M.E., 2019. Draxin alters laminin organization during basement membrane remodeling to control cranial neural crest EMT. Developmental biology 446, 151-158.

Hutchins, E.J., Piacentino, M.L., Bronner, M.E., 2020. P-bodies are sites of rapid RNA decay during the neural crest epithelial—mesenchymal transition, BioRxiv, 2020.07.31.231860.

Hutchins, E.J., Piacentino, M.L., Bronner, M.E., 2021. Transcriptomic Identification of Draxin-Responsive Targets During Cranial Neural Crest EMT. Front Physiol 12, 624037.

Hutchins, E.J., Szaro, B.G., 2013. c-Jun N-terminal kinase phosphorylation of heterogeneous nuclear ribonucleoprotein K regulates vertebrate axon outgrowth via a posttranscriptional mechanism. The Journal of neuroscience : the official journal of the Society for Neuroscience 33, 14666-14680.

Jayaseelan, S., Doyle, F., Tenenbaum, S.A., 2014. Profiling post-transcriptionally networked mRNA subsets using RIP-Chip and RIP-Seq. Methods 67, 13-19.

Kalev-Altman, R., Hanael, E., Zelinger, E., Blum, M., Monsonego-Ornan, E., Sela-Donenfeld, D., 2020. Conserved role of matrix metalloproteases 2 and 9 in promoting the migration of neural crest cells in avian and mammalian embryos. FASEB J 34, 5240-5261.

Katsanou, V., Milatos, S., Yiakouvaki, A., Sgantzis, N., Kotsoni, A., Alexiou, M., Harokopos, V., Aidinis, V., Hemberger, M., Kontoyiannis, D.L., 2009. The RNA-binding protein Elavl1/HuR is essential for placental branching morphogenesis and embryonic development. Molecular and cellular biology 29, 2762-2776.

Keene, J.D., 2007. RNA regulons: coordination of post-transcriptional events. Nat Rev Genet 8, 533-543.

Keene, J.D., Tenenbaum, S.A., 2002. Eukaryotic mRNPs may represent posttranscriptional operons. Mol Cell 9, 1161-1167.

Kim, I., Hur, J., Jeong, S., 2015. HuR represses Wnt/beta-catenin-mediated transcriptional activity by promoting cytoplasmic localization of beta-catenin. Biochem Biophys Res Commun 457, 65-70.

Langmead, B., Salzberg, S.L., 2012. Fast gapped-read alignment with Bowtie 2. Nature methods 9, 357-359.

Liu, L., Ouyang, M., Rao, J.N., Zou, T., Xiao, L., Chung, H.K., Wu, J., Donahue, J.M., Gorospe, M., Wang, J.Y., 2015. Competition between RNA-binding proteins CELF1 and HuR modulates MYC translation and intestinal epithelium renewal. Mol Biol Cell 26, 1797-1810.

Ma, W.J., Cheng, S., Campbell, C., Wright, A., Furneaux, H., 1996. Cloning and characterization of HuR, a ubiquitously expressed Elav-like protein. The Journal of biological chemistry 271, 8144-8151.

Manohar, S., Camacho, A., Rogers, C.D., 2020. Cadherin-11 is required for neural crest determination and survival. bioRxiv, 2020.2005.2018.066613.

Martik, M.L., Bronner, M.E., 2017. Regulatory Logic Underlying Diversification of the Neural Crest. Trends Genet.

Martin, M., 2011. Cutadapt removes adapter sequences from high-throughput sequencing reads. 2011 17, 3.

Megason, S.G., McMahon, A.P., 2002. A mitogen gradient of dorsal midline Wnts organizes growth in the CNS. Development 129, 2087-2098.

Milet, C., Monsoro-Burq, A.H., 2012. Neural crest induction at the neural plate border in vertebrates. Developmental biology 366, 22-33.

Monier-Gavelle, F., Duband, J.L., 1995. Control of N-cadherin-mediated intercellular adhesion in migrating neural crest cells in vitro. J Cell Sci 108 (Pt 12), 3839-3853.

Monsonego-Ornan, E., Kosonovsky, J., Bar, A., Roth, L., Fraggi-Rankis, V., Simsa, S., Kohl, A., Sela-Donenfeld, D., 2012. Matrix metalloproteinase 9/gelatinase B is required for neural crest cell migration. Developmental biology 364, 162-177.

Mukherjee, N., Corcoran, David L., Nusbaum, Jeffrey D., Reid, David W., Georgiev, S., Hafner, M., Ascano, M., Tuschl, T., Ohler, U., Keene, Jack D., 2011. Integrative Regulatory Mapping Indicates that the RNA-Binding Protein HuR Couples Pre-mRNA Processing and mRNA Stability. Molecular Cell 43, 327-339.

Pabis, M., Popowicz, G.M., Stehle, R., Fernández-Ramos, D., Asami, S., Warner, L., García-Mauriño, S.M., Schlundt, A., Martínez-Chantar, M.L., Díaz-Moreno, I., Sattler, M., 2018. HuR biological function involves RRM3-mediated dimerization and RNA binding by all three RRMs. Nucleic acids research 47, 1011-1029.

Piacentino, M.L., Hutchins, E.J., Bronner, M.E., 2021. Essential function and targets of BMP signaling during midbrain neural crest delamination. Developmental biology 477, 251-261.

Rabadán, M.A., Herrera, A., Fanlo, L., Usieto, S., Carmona-Fontaine, C., Barriga, E.H., Mayor, R., Pons, S., Marti, E., 2016. Delamination of neural crest cells requires transient and reversible Wnt inhibition mediated by Dact1/2. Development 143, 2194-2205.

Rothamel, K., Arcos, S., Kim, B., Reasoner, C., Lisy, S., Mukherjee, N., Ascano, M., 2021. ELAVL1 primarily couples mRNA stability with the 3' UTRs of interferon-stimulated genes. Cell Rep 35, 109178.

Sanchez-Vasquez, E., Bronner, M.E., Strobl-Mazzulla, P.H., 2019. Epigenetic inactivation of miR-203 as a key step in neural crest epithelial-to-mesenchymal transition. Development 146.

Scotto-Lavino, E., Du, G., Frohman, M.A., 2006. 3' end cDNA amplification using classic RACE. Nature protocols 1, 2742-2745.

Shi, B., Zhang, J., Heng, J., Gong, J., Zhang, T., Li, P., Sun, B.F., Yang, Y., Zhang, N., Zhao, Y.L., Wang, H.L., Liu, F., Zhang, Q.C., Yang, Y.G., 2020. RNA structural dynamics regulate early embryogenesis through controlling transcriptome fate and function. Genome Biol 21, 120.

Simoes-Costa, M., Bronner, M.E., 2015. Establishing neural crest identity: a gene regulatory recipe. Development 142, 242-257.

Simoes-Costa, M., Stone, M., Bronner, M.E., 2015. Axud1 Integrates Wnt Signaling and Transcriptional Inputs to Drive Neural Crest Formation. Developmental cell 34, 544-554.

Steventon, B., Mayor, R., 2012. Early neural crest induction requires an initial inhibition of Wnt signals. Developmental biology 365, 196-207.

Strobl-Mazzulla, P.H., Bronner, M.E., 2012. A PHD12-Snail2 repressive complex epigenetically mediates neural crest epithelial-to-mesenchymal transition. The Journal of cell biology 198, 999-1010.

Taneyhill, L.A., Coles, E.G., Bronner-Fraser, M., 2007. Snail2 directly represses cadherin6B during epithelial-to-mesenchymal transitions of the neural crest. Development 134, 1481-1490.

Tribulo, C., Aybar, M.J., Nguyen, V.H., Mullins, M.C., Mayor, R., 2003. Regulation of Msx genes by a Bmp gradient is essential for neural crest specification. Development 130, 6441-6452.

Tutucci, E., Vera, M., Biswas, J., Garcia, J., Parker, R., Singer, R.H., 2018. An improved MS2 system for accurate reporting of the mRNA life cycle. Nature methods 15, 81-89.

van Limborgh, J., Lieuw Kie Song, S.H., Been, W., 1983. Cleft lip and palate due to deficiency of mesencephalic neural crest cells. Cleft Palate J 20, 251-259.

Vega-Lopez, G.A., Cerrizuela, S., Tribulo, C., Aybar, M.J., 2018. Neurocristopathies: New insights 150 years after the neural crest discovery.

Developmental biology.

Ward, N.J., Green, D., Higgins, J., Dalmay, T., Munsterberg, A., Moxon, S., Wheeler, G.N., 2018. microRNAs associated with early neural crest development in Xenopus laevis. BMC Genomics 19, 59.

Weiner, A.M.J., 2018. MicroRNAs and the neural crest: From induction to differentiation. Mechanisms of development 154, 98-106.

Williams, R.M., Candido-Ferreira, I., Repapi, E., Gavriouchkina, D., Senanayake, U., Ling, I.T.C., Telenius, J., Taylor, S., Hughes, J., Sauka-Spengler, T., 2019. Reconstruction of the Global Neural Crest Gene Regulatory Network In Vivo. Developmental cell 51, 255-276 e257.

Wu, J., Saint-Jeannet, J.P., Klein, P.S., 2003. Wnt-frizzled signaling in neural crest formation. Trends Neurosci 26, 40-45.

Yanfeng, W., Saint-Jeannet, J.P., Klein, P.S., 2003. Wnt-frizzled signaling in the induction and differentiation of the neural crest. Bioessays 25, 317-325.

Yao, K.M., Samson, M.L., Reeves, R., White, K., 1993. Gene elav of Drosophila melanogaster: a prototype for neuronal-specific RNA binding protein gene family that is conserved in flies and humans. Journal of neurobiology 24, 723-739.

Yuan, Z., Sanders, A.J., Ye, L., Wang, Y., Jiang, W.G., 2011. Knockdown of human antigen R reduces the growth and invasion of breast cancer cells in vitro and affects expression of cyclin D1 and MMP-9. Oncol Rep 26, 237-245.

Zuker, M., 2003. Mfold web server for nucleic acid folding and hybridization prediction. Nucleic acids research 31, 3406-3415.

Key Resources Table

Reagent type (species) or resource	Designation	Source or reference	Identifiers	Additional information
Gene (*Gallus gallus*)	*Elavl1*	GenBank	NM_204833.1	
Gene (Gallus gallus)	*Draxin*	GenBank	AB427147.1	
Gene (Gallus gallus)	*Axud1 (CSRNP1)*	This paper	GenBank: ON920861	3'-untranslated region
Gene (Gallus gallus)	*Msx1*	Ensembl	ENSGALT00000024209.4	
Gene (Gallus gallus)	*BMP4*	Ensembl	ENSGALT00000020316.7	
Gene (Gallus gallus)	*Tfap2b*	Ensembl	ENSGALT00000026916.6	
Gene (Gallus gallus)	*Pax7*	Ensembl	ENSGALT00000048594.2	
strain, strain background (Gallus gallus)	Rhode Island Red	Sun State Ranch (Monrovia, CA, USA)		
antibody	Rabbit anti-Elavl1	Abcam	Cat# ab196626	1:100 immunohistochemistry; 5 µg immunoprecipitation
antibody	Mouse IgG1 anti-Pax7	Developmental Studies Hybridoma Bank	Cat# pax7, RRID:AB_528428	1:5
antibody	Goat IgG anti-GFP	Rockland	Cat# 600-101-215, RRID:AB_218182	1:500
antibody	Rabbit IgG, polyclonal - Isotype Control (ChIP Grade)	Abcam	Cat# ab171870	5 µg immunoprecipitation
recombinant DNA reagent	pCI-H2B-RFP (plasmid)	Betancur et al., 2010	N/A	
recombinant DNA reagent	pCIG (plasmid)	Megason and McMahon, 2002	N/A	
recombinant DNA reagent	Draxin-FLAG (plasmid)	Hutchins and Bronner, 2018	N/A	
recombinant DNA reagent	MCP-GFP (plasmid)	Hutchins et al., 2020	N/A	
recombinant DNA reagent	MS2-Draxin 3'UTR (plasmid)	This paper; Hutchins et al., 2020	N/A	
sequence-based reagent	Control morpholino	GeneTools	N/A	5'-CCTCTTACCTCAGTTACAATTTATA
sequence-based reagent	Elavl1 morpholino	This paper; GeneTools	N/A	5'-GACATCTTATAACGTATCTCGCTGC
sequence-based reagent	Draxin morpholino	Hutchins and Bronner, 2018; GeneTools	N/A	5'-AAGGTGGAAGAAGCTGCCATAATCC
sequence-based reagent	Draxin qPCR primers	This paper; IDT	Custom DNA oligos	Forward: 5'-CTACGCTGTTATGCCAAATTCC; Reverse: 5'-GAATGATCCCTGCTCTCCATT
sequence-based reagent	Axud1 qPCR primers	This paper; IDT	Custom DNA oligos	Forward: 5'-TCCAGTCCTTCTCGGACTATAA; Reverse: 5'-GGGAAATTAGGCAACTGAAACTG
sequence-based reagent	Msx1 qPCR primers	This paper; IDT	Custom DNA oligos	Forward: 5'-AGCTGGAGAAGCTGAAGATG; Reverse: 5'-AGGCTCCGTACAGGGAT
sequence-based reagent	BMP4 qPCR primers	This paper; IDT	Custom DNA oligos	Forward: 5'-TTGGTCAACTCCGTCAACTC; Reverse: 5'-CAGCACCACCTTGTCATACT
sequence-based reagent	Pax7 qPCR primers	This paper; IDT	Custom DNA oligos	Forward: 5'-CAAACCAACTCGCAGCATTC; Reverse: 5'-CTGCCTCCATCTTGGGAAAT
sequence-based reagent	FoxD3 qPCR primers	This paper; IDT	Custom DNA oligos	Forward: 5'-CATCTGCGAGTTCATCAGCA; Reverse: 5'-TTCACGAAGCAGTCGTTGAG
sequence-based reagent	3'-RACE QT primer	Scotto-Lavino et al., 2006; IDT	Custom DNA oligos	5'-CCAGTGAGCAGAGTGACGAGGACTCGAGCTCAAGCTTTTTTTTTTTTTTTTT
sequence-based reagent	3'-RACE QO primer	Scotto-Lavino et al., 2006; IDT	Custom DNA oligos	5'-CCAGTGAGCAGAGTGACG
sequence-based reagent	3'-RACE QI primer	Scotto-Lavino et al., 2006; IDT	Custom DNA oligos	5'-GAGGACTCGAGCTCAAGC
sequence-based reagent	3'-RACE Axud1 Gene Specific Primer 1	This paper; IDT	Custom DNA oligos	5'-CGTGTTCCAAGAGCTATGCC
sequence-based reagent	3'-RACE Axud1 Gene Specific Primer 2	This paper; IDT	Custom DNA oligos	5'-GGTTTCCCGCAAGCTGG
commercial assay or kit	RNAqueous-Micro Total RNA isolation kit	Ambion	Cat# AM1931	
commercial assay or kit	SMART-Seq v4 Ultra Low Input cDNA kit	Takara Bio	Cat# 634889	
commercial assay or kit	Agencourt AMPure XP beads	Beckman Coulter	Cat# A63880	
commercial assay or kit	Endofree maxi prep kit	Qiagen	Cat# 12362	
commercial assay or kit	Duolink® In Situ PLA Probe Anti-Rabbit MINUS	Millipore/Sigma	Cat# DUO92005	
commercial assay or kit	Duolink® In Situ PLA Probe Anti-Goat PLUS	Millipore/Sigma	Cat# DUO92003	
commercial assay or kit	Duolink® In Situ Detection Reagents FarRed	Millipore/Sigma	Cat# DUO92013	
commercial assay or kit	Duolink® In Situ Wash Buffers, Fluorescence	Millipore/Sigma	Cat# DUO82049	
chemical compound, drug	Duolink® In Situ Mounting Medium with DAPI	Millipore/Sigma	Cat# DUO82040	
chemical compound, drug	Fluoromount-G	SouthernBiotech	Cat# 0100-01	
chemical compound, drug	DAPI	Thermo Fisher	Cat# D1306	1:5000
chemical compound, drug	FastStart Universal SYBR Green Master (Rox)	Millipore/Sigma	Cat# FSUSGMMRO	
chemical compound, drug	SuperScript III Reverse Transcriptase	Thermo Fisher	Cat# 18080044	
chemical compound, drug	cOmplete, Mini, EDTA-free Protease Inhibitor	Millipore/Sigma	Cat# 11836170001	
chemical compound, drug	RNaseOUT Recombinant Ribonuclease Inhibitor	Thermo Fisher	Cat# 10777019	
chemical compound, drug	Accumax	Innovative Cell Technologies, Inc	Cat# AM105	
chemical compound, drug	Protein G Dynabeads	Thermo Fisher	Cat# 10003D	
chemical compound, drug	Actinomycin D	Millipore/Sigma	Cat# A9415	10 µg/mL
software, algorithm	Fiji	Schindelin et al., 2012	RRID:SCR_002285	https://imagej.net/Fiji
software, algorithm	Seurat	Butler et al., 2018	RRID:SCR_007322	https://satijalab.org/seurat/
software, algorithm	QuantStudio Design & Analysis software, version 2.4	Life Technologies	RRID:SCR_018712	
software, algorithm	Zen 2 Blue	Zeiss	N/A	
software, algorithm	Zen Black	Zeiss	N/A	
software, algorithm	Photoshop CC	Adobe	N/A	
software, algorithm	Prism8, Prism9	GraphPad	N/A	
software, algorithm	FastQC	Andrews, 2014	RRID:SCR_014583	
software, algorithm	Cutadapt	Martin, 2011	RRID:SCR_011841	
software, algorithm	Bowtie2	Langmead and Salzberg, 2012	RRID:SCR_016368	
software, algorithm	HTSeq-Count	Anders et al., 2015	RRID:SCR_011867	
software, algorithm	biomaRt package	Durinck et al., 2009	RRID:SCR_019214	
software, algorithm	mfold	Zuker, 2003	RRID:SCR_008543	
software, algorithm	G*Power	Faul et al., 2007	RRID:SCR_013726	
other, deposited data	sc-RNA (SmartSeq2)	Williams et al., 2019	GEO: GSE130500	
other, deposited data	RNA-seq data (bulk)	This paper	NCBI Bioproject: PRJNA861325	Single-end RNA-Sequencing datasets

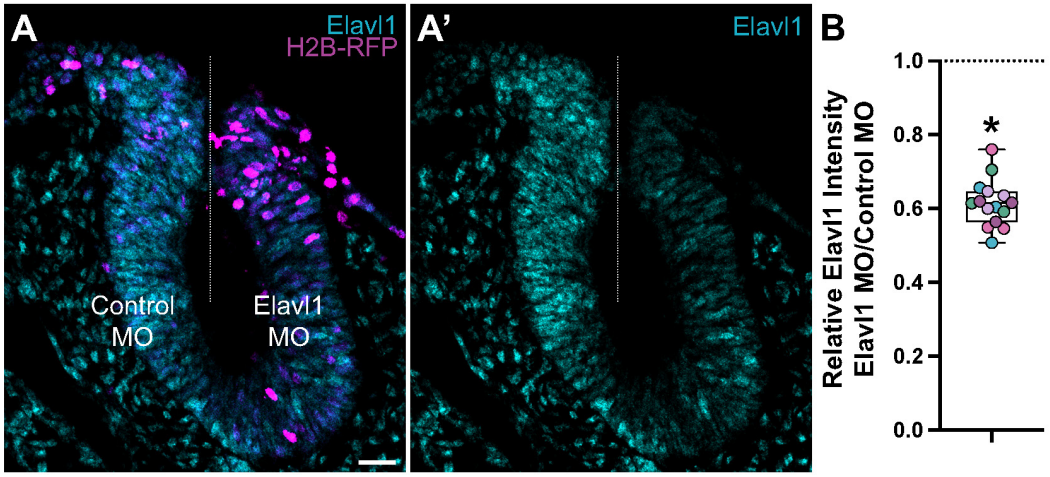

Figure 3—Figure Supplement 1. Translation-blocking morpholino suppresses Elavl1 expression.
(**A**) Representative apotome maximum intensity projection micrograph of cross-sectioned embryo bilaterally co-electroporated with a fluorescent electroporation control construct (H2B-RFP) and control morpholino (left) or Elavl1 morpholino (right), immunostained for Elavl1 (cyan). Dotted white line indicates midline. MO, morpholino. Scale bar, 20 µm. (**B**) Relative fluorescence intensity of Elavl1 for Elavl1 knockdown compared to control sides of cross-sections, calculated as ratio of Elavl1 morpholino versus control morpholino integrated density. Data are from individual sections; sections from same embryo are displayed in same color (n = 5 embryos, 15 sections) *, $P < 0.001$, paired t-test.

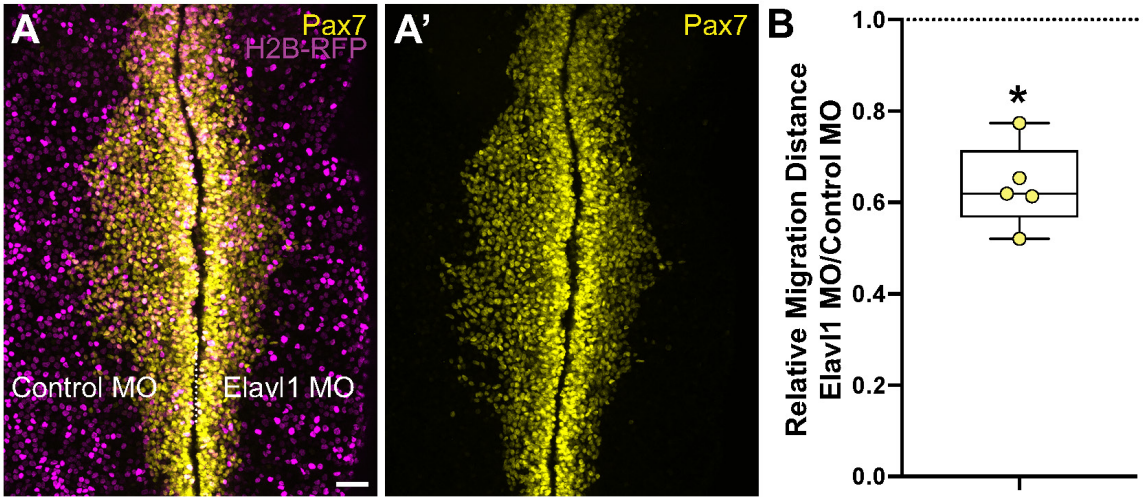

Figure 3—Figure Supplement 2. Elavl1 knockdown inhibits cranial neural crest emigration.
(**A**) Representative confocal maximum intensity projection micrograph of whole mount embryo bilaterally co-electroporated with a fluorescent electroporation control construct (H2B-RFP) and control morpholino (left) or Elavl1 morpholino (right), immunostained for Pax7 (yellow). Dotted white line indicates midline. MO, morpholino. Scale bar, 50 µm. (**B**) Relative migration distance for electroporated sides compared to control sides of whole mount embryos, calculated as ratio. Data are from individual embryos (n = 5 embryos, 5 measurements per embryo averaged). *, $P < 0.001$, Wilcoxon matched-pairs signed rank test).

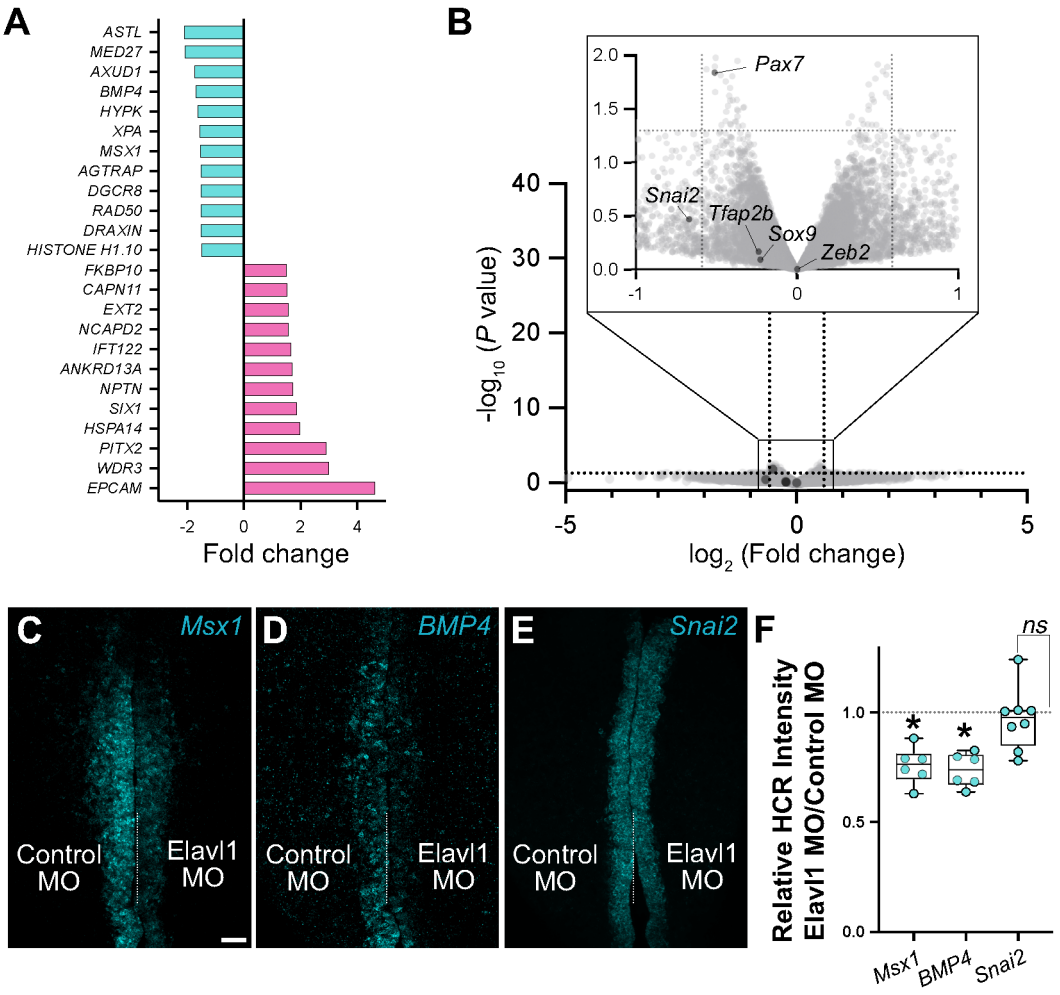

Figure 4—Figure Supplement 1. RNA-sequencing identified four neural crest genes specifically downregulated with Elavl1 knockdown.

(**A-B**) Although RNA-sequencing (RNA-seq) identified four genes with established roles in neural crest development (*Draxin*, *Axud1*, *Msx1*, *BMP4*) that were significantly downregulated with Elavl1 knockdown (**A**), several other neural crest genes were unaffected (**B**). (**B**) Volcano plot of genes that were not significantly different for Elavl1 knockdown versus control, with known neural crest genes *Pax7*, *Tfab2b*, *Snai2*, *Sox9*, and *Zeb2* indicated. (**C-E**) Representative confocal maximum intensity projection micrographs of HCR processed embryos for *Msx1* (**C**), *BMP4* (**D**), *Snai2* (**E**). (**F**) Quantitation of HCR processed embryos for control versus Elavl1 knockdown, calculated as ratio of Elavl1 MO versus control MO integrated density. Dotted white line indicates midline. MO, morpholino. Scale bar, 50 µm. *, $P < 0.001$; *ns*, non-significant, $P = 0.54$; one sample *t*-test.

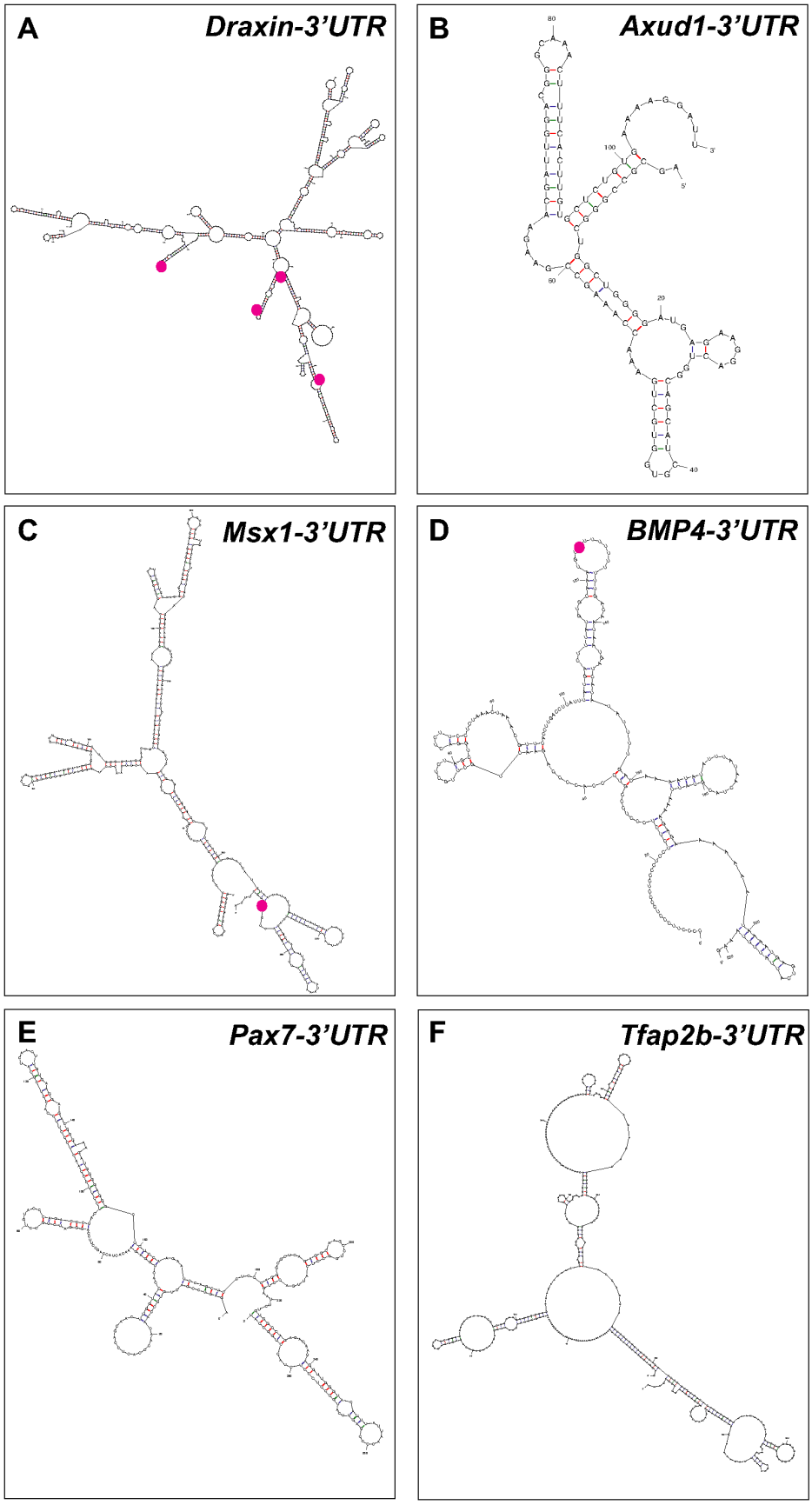

Figure 4—Figure Supplement 2. Putative Elavl1 binding sites within the Draxin 3'-untranslated region predicts a direct interaction.

(**A-F**) Representative secondary structures of the *Draxin* 3'-untranslated region (UTR) (**A**), *Axud1* 3'-UTR (**B**), *Msx1* 3'-UTR (**C**), *BMP4* 3'-UTR (**D**), *Pax7* 3'-UTR (**E**), and *Tfap2b* 3'-UTR (**F**), predicted by 'mfold' analysis. Predicted Elavl1 binding sites are highlighted using magenta dots.